2002

Submitted to: Journal of the Acoustical Society of America

# Broadband acoustic backscatter and high-resolution morphology of fish: Measurement and modeling

D. Benjamin Reeder[1], J. Michael Jech[2] and Timothy K. Stanton[1]

[1] *Woods Hole Oceanographic Institution, Woods Hole, Massachusetts 02543*

[2] *NOAA/NMFS Northeast Fisheries Science Center, Woods Hole, MA 02543*

PACS numbers: 43.30.Sf, 43.30.Ft, 43.30.Xm

Remote detection and classification of marine organisms require accurate acoustic scattering models that adequately incorporate organism morphology. Broadband acoustic backscattering measurements, advanced high-resolution imaging of fish morphology using CT scans and phase-contrast x-rays (in addition to traditional x-rays), and associated scattering modeling using the images have been conducted involving alewife (*Alosa pseudoharengus*), a swimbladder-bearing fish. A greater-than-octave bandwidth (40-95 kHz), shaped, linearly swept, frequency modulated signal was used to insonify live, individual, adult alewife that were tethered while being rotated in 1-degree increments of orientation angle over all angles in two planes of rotation (lateral and dorsal/ventral). These data, in addition to providing the orientation dependence of the scattering over a continuous band of frequencies, were also used (after pulse compression) to identify the dominant scattering features of the fish (including the skull and swimbladder). The x-ray and CT scan images of the swimbladder were digitized and incorporated into two scattering models: one is the Kirchhoff-Ray Mode (KRM) model [Clay and Horne, 1994], and the other is the conformal-mapping-based

Fourier Matching Method (FMM), which has recently been extended to finite-length bodies [Reeder and Stanton, submitted]. The comparison between the scattering predictions and data demonstrate the utility of the CT scan imagery for use in scattering modeling, as it provided a means for rapidly and non-invasively measuring the fish morphology in three dimensions and at high resolution. In addition to further validation of the KRM model, the potential of the new FMM formulation was demonstrated, which is a versatile approach, valid over a wide range of shapes, all frequencies and all angles of orientation. Recommendations for future modeling, based on the above comparison and the acoustic observation of multiple scattering features of the fish, are given.

## I. INTRODUCTION

Acoustic methods have long been used to rapidly and synoptically survey marine organisms of ecological and economic importance. Acoustic methods complement traditional methods such as direct sampling with nets. Direct sampling furnishes biological data such as abundance, biomass, direct measurements of organism size and species identification, but encounters problems such as net avoidance, small sampling volumes, catch destruction of delicate specimens, and costs in time and money. Acoustically surveying the organisms could avoid these problems, particularly in the case of large-scale synoptic surveys that require high-resolution data (Gunderson, 1993; Medwin and Clay, 1998). Since acoustic sampling does not directly produce biological data, inference of biological information from acoustic scattering by marine organisms requires an understanding of the process by which those organisms scatter sound.

Understanding the scattering mechanisms of marine organisms is a challenge due to the fact

that fish anatomy is complex and the acoustic scattering characteristics are correspondingly complex. Nash *et al.* (1987) illustrated the influence of the various anatomical components of fish on the scattering by performing length-wise acoustic scans of whole fish and dissected swimbladders, heads and vertebrae (Fig. 1). Given the complexities of the scattering characteristics of marine organisms as illustrated in that and other studies, detailed investigations must be made into the scattering mechanisms of the animals in order to determine and decipher the extent to which each dependency contributes to the overall scattering characteristics. Studies must consist of careful, accurate measurement of the acoustic scattering and associated modeling to effectively elucidate these mechanisms. Due to the large number of organisms that exist in the ocean, it is not possible to study the scattering by all species; however, organisms can generally be categorized according to morphological groups. For example, fish can be categorized by morphological characteristics, such as size, shape and the presence or absence of swimbladders (Foote, 2001). Regarding zooplankton, Stanton *et al.* (1994, 1998a, 1998b) identified three major categories: fluid-like (e.g., euphausiids, shrimp, copepods), gas inclusions (e.g., siphonophores), and elastic shells (e.g., pteropods).

Much research has been directed toward making measurements of the scattering of sound by fish, usually in terms of target strength (Midttun, 1984; Foote, 2001). Studies have included measurement of target strengths *in situ* and *ex situ*, with both multiple and single targets. *In situ* measurements present the challenge of unknown target size, orientation and sometimes position relative to the acoustic beam, while *ex situ* measurements provide greater control over these factors, although in an unnatural environment (Foote, 1997). *Ex situ* measurements of tethered fish include those conducted by Jones and Pearce (1958), Haslett (1969), Diercks

and Goldsberry (1970), Love (1969, 1970, 1971), Nakken and Olson (1977), Miyanohana *et al.* (1990), and Benoit-Bird and Au (2001). Although most of these measurements were performed at single frequencies and at a limited number of angles of orientation (mostly dorsal), they were performed on a variety of species of different sizes and demonstrate complicated variability that is dependent upon morphology, orientation and acoustic wavelength. Attempts have been made to empirically quantify the relationship between echo amplitude and actual fish length (Love, 1977; Foote, 1987). Although linear regression curves have been used with some success, they are constrained to certain ranges of frequencies and species and lack the ability to make predictions outside those bounds (Horne and Jech, 1999). Scattering models of greater sophistication have been required to better account for the complexities introduced by shape, orientation and material properties.

Modeling of the scattering of sound by complex body shapes is a difficult problem due to the mathematical challenge of exact solutions and the computational difficulties of numerical approaches. A number of approaches have been used to represent the shape of the dominant scattering mechanisms. For low frequency applications, the acoustically dominant swimbladder has been modeled as a sphere (Andreyeva, 1964; Love, 1978; Ye and Farmer, 1994; Feuillade and Nero, 1998) and as a prolate spheroid (Weston, 1967). At high frequencies, the elongation of the scatterers has increasing importance and efforts in this frequency region have been made to describe the scattering by more realistic, irregular shapes. For example, Jones and Pearce (1957) and Haslett (1962) attempted to experimentally approximate the shape of a fish swimbladder as a cylinder and ellipsoid, respectively, and Do and Surti (1990) used a series of cylinders and cones in a similar fashion. Furusawa (1988) and Ye (1996) modeled acoustic scattering by fish using

prolate spheroids. Arrays of point scatterers (Clay and Heist, 1984) have been used to model the fish body form. Foote (1985) computed the target strength of fish by applying the Kirchhoff approximation to a realistic 3-dimensional model of the swimbladder based on the digitized microtomed swimbladders of pollack (*Pollachius pollachius*) and saithe (*Pollachius virens*). Clay (1991) combined a component of Stanton's (1988, 1989) deformed finite cylinder model (based on a modal series solution) in the low frequency region with the Kirchhoff approximation for high frequencies to create the Kirchhoff-ray mode (KRM) model to account for the irregular shape of the swimbladder and fish body and make predictions over all frequencies. Clay and Horne (1994) modeled acoustic backscatter of Atlantic cod (*Gadus morhua*) using the KRM model. Foote and Francis (2002) modeled the target strength of swimbladdered fish using the boundary element method based on the same swimbladder shapes in Foote (1985). Models using the exact shape of the animals' morphology are desired because they are more realistic and promise greater accuracy over models based on simple geometric shapes, especially in the geometric scattering region (high $ka$). Each of the above-mentioned scattering models are limited with respect to frequency range, class of surfaces, types of boundary conditions, eccentricity of shape and/or numerical efficiency.

As shown in the above studies, successful use of acoustics in ocean observations requires accurate scattering models for each category of animal, verification and refinement of the models through accurate, extensive measurements of scattering from fish, and reliable algorithms for numerical implementation of the models. Very importantly, advanced scattering models must include scatterer shapes that closely resemble the dominant scattering features within the fish. This information requires high-resolution morphological measurements of the fish to be made.

Another important requirement is that the acoustic scattering measurements be conducted over a wide range of frequencies, preferably with continuous coverage over the frequency band.

In spite of the need for broad spectral coverage in the scattering measurements, the majority of acoustic measurements on fish are in terms of target strengths at single frequencies. Although this level of information has been proven to be very useful for certain applications, such as fishery population estimates, traditional target strength measurements lack spectral coverage for rigorous model development. Specifically, narrowband measurements are performed at discrete frequencies, thus frequency dependencies are missing from the data, although this has been addressed, in part, by use of multiple discrete frequencies. Since an animal's scattering properties vary considerably with the frequency of the transmitted signal, the use of broadband transducers offer continuous coverage over a significant range of frequencies, thus increasing the amount of information contained in the signal. Furthermore, the broadband signals inherently have high temporal resolution (which varies with inverse bandwidth of the transmitted signal) which can be realized through the use of an impulse signal or pulse compression of a longer signal (Chu and Stanton, 1998). With high temporal resolution, scattering features can possibly be resolved in time and identified. In spite of the great advantages of broadband signals, relatively few studies have investigated and/or exploited the animal's spectral characteristics (Kjaergaard *et al.*, 1990; Simmonds *et al.*, 1996; Zakharia *et al.*, 1996).

The needs for broadband acoustic measurements and advanced scattering models that incorporate high-resolution morphology are addressed in this study. Extensive broadband acoustic measurements were conducted on live, adult alewife (*Alosa pseudoharengus*), which were tethered while being rotated in 1-degree increments of orientation angle over all angles in two planes

of rotation (lateral and dorsal/ventral). Spectral and time-domain analyses identify dominant scattering mechanisms and demonstrate the extent to which the scattering depends on size, shape, acoustic frequency and orientation angle. Traditional x-rays and advanced techniques involving CT scans were used to rapidly and non-invasively image the anatomy of the fish so that digitizations of swimbladder shape could be incorporated into two scattering models—the KRM model referenced above (using traditional x-rays), as well as a newly developed scattering formulation, the Fourier Matching Method (FMM) for axisymmetric finite-length bodies (Reeder and Stanton, submitted). The FMM formulation, which incorporated the CT scan images, is a versatile, numerically efficient model applicable over a wide range of shapes, all angles and all frequencies. Predictions by the two scattering models, using the morphological information, are compared to the acoustical backscattering laboratory measurements of the alewife.

This paper is organized as follows. In Sec. II, basic descriptions of target strength and pulse compression (PC) processing of broadband signals are given, followed by a synopsis of the Kirchhoff-Ray Mode and Fourier Matching Method models. In Sec. III, the laboratory setup, methods used for data collection and measurements of animal morphology are presented. Acoustic scattering results are presented in Sec. IV. Comparisons between model predictions and measurements are made in Sec. V, followed by a discussion and conclusions in Sec. VI.

## II. THEORY

## A. Definitions

The far-field scattered sound wave is expressed as:

$$P^{scat} \underset{r\to\infty}{\rightarrow} P^{inc}\frac{e^{ikr}}{r}f, \tag{1}$$

where $P^{inc}$ is the pressure amplitude of the acoustic wave incident upon the object, $r$ is the distance between the object and receiver, $k$ ($= 2\pi/\lambda$, where $\lambda$ = wavelength) is the acoustic wavenumber of the incident field, and $f$ is the scattering amplitude. The far-field scattering characteristics of the object are fully described by the scattering amplitude. Given the sometimes large dynamic range of the scattering amplitude, it is often expressed in logarithmic terms for the case of backscatter as target strength (TS), expressed in units of decibels (dB) relative to 1 m (Urick, 1983):

$$TS = 10\log_{10}|f_{bs}|^2 = 10\log_{10}\sigma_{bs}, \tag{2}$$

where $\sigma_{bs} \equiv |f_{bs}|^2$ is the differential backscattering cross section and differs from the often-used backscattering cross section , $\sigma$, by a factor of $4\pi$ ($\sigma = 4\pi\sigma_{bs}$). The term, $f_{bs}$, is the scattering amplitude evaluated in the backscatter direction. Target strength is often normalized by the square of some typical dimension to give the reduced target strength (RTS):

$$RTS = 10\log_{10}\left|\frac{\sigma_{bs}}{L^2}\right| = 10\log_{10}|f_{bs}|^2 - 10\log_{10}L^2, \tag{3}$$

where $L$ is, in the case of elongated scatterers, the length of the scattering object. In the case of a sphere, the target strength is often normalized by $\pi a^2$ instead of $L^2$. The average target

strength is expressed in terms of the value of the average backscattering cross section:

$$\langle TS \rangle = 10 \log_{10} \langle \sigma_{bs} \rangle , \tag{4}$$

where the average in this study, denoted $\langle ... \rangle$, is performed over the frequency band and before the logarithm operation is performed.

## B. Pulse compression

In order to resolve major scattering features such as the skull and swimbladder of the fish, the received signal is compressed in time by cross correlating the echo with the received calibration signal. The result is a short, high-amplitude signal with increased signal-to-noise ratio (SNR). This type of process is particularly effective for long, wideband signals such as those used in this study. This approach is similar to the commonly used matched filter that involves cross correlating the received signal plus noise with the original signal without the noise (Turin, 1960). In the case of scattering from marine organisms, however, the exact scattering characteristics of the animal are not known; therefore, the "replicate" signal (corresponding to the signal without the noise) used in the correlation process for a true matched filter, is not known. Chu and Stanton (1998) suggested using a different signal in the cross-correlation: the received signal obtained during calibration. This modified matched filter process is referred to as pulse compression and its output is referred to as the compressed pulse output (CPO). The resultant output is a series of echoes, corresponding to the dominant scattering features of the target.

## C. Models

Two scattering models that are valid for elongated scatterers and for a wide range of fre-

quencies and orientations are used to compare with the experimental data: the Kirchhoff-Ray Mode (KRM) model which has previously been applied to fish and the newly developed Fourier Matching Method (FMM).

## 1. KRM

The Kirchhoff-Ray Mode (KRM) model has been used to compute the scattering from fish with a hybrid approach by predicting the scattering by the swimbladder in the low $ka$ region with a monopole ($m = 0$) mode to a cylinder solution and predicting the scattering by the swimbladder and fish body in the high $ka$ region with the Kirchhoff, or "ray", approximation. For both components of the solution, the scattering object is approximated by a series of 1-mm long cylindrical elements constructed from the digitized shape of the body and swimbladder using traditional x-ray images. The cross-sectional radius, $a$, is half of the width of each cylindrical element.

For the swimbladder scattering in the low $ka$ region ($ka < 0.15$), the cylindrical monopole solution is written as the sum of the scatter from $N_e$ elements:

$$f_{bs}^{(sb)} = \frac{-i}{\pi} \sum_{j=1}^{N_e} b_0 e^{-i2kv(j)} dx(j), \qquad (ka < 0.15) \tag{5}$$

where $f_{bs}^{(sb)}$ is the backscattering amplitude as a function of frequency (notation of $\mathcal{L}$ in Clay and Horne (1994) is replaced by $f_{bs}^{(sb)}$), $b_0$ is the zero-order mode scattering coefficient, $v(j)$ is the displacement from the central axis of the fish to the outer boundary of the surface, and $dx$ is the incremental distance along the length of the object. For the swimbladder scattering in the high $ka$ region ($ka > 0.15$), the Kirchhoff ray approximation is used. An equation similar in form to

the above equation is used to sum the backscattered rays from $N_e$ swimbladder elements:

$$f_{bs}^{(sb)} = -i\frac{R_{fs}(1-R_{wf}^2)}{2\sqrt{\pi}} \sum_{j=0}^{N_e-1} A_{sb}(k_{fb}a(j)+1)^{1/2} e^{-i(2k_{fb}v_U(j)+\Psi_{sb})} dx(j), \qquad (ka > 0.15) \quad (6)$$

where $R_{fs}$ is the reflection coefficient, $U$ and $L$ indicate the upper and lower surfaces, $wf$ refers to the water-fish interface, $fs$ denotes the swimbladder-fish body interface, $fb$ denotes the fish body, $sb$ refers to the swimbladder, and $A_{sb}$ and $\Psi$ are previously determined empirical amplitude and phase adjustments for small $ka$. A similar expression using the Kirchhoff approximation describes the scattering for the fish body in the high $ka$ region ($ka > 0.15$):

$$\begin{aligned} f_{bs}^{(fb)} \;=\; & -i\frac{R_{wf}}{2\sqrt{\pi}} \sum_{j=0}^{N_e-1} \{(ka(j))^{1/2} \qquad (ka > 0.15) \\ & \times [e^{-i(2kv_U(j)} - (1-R_{wf}^2) e^{i(-2kv_U(j)+2k_{fb}(v_U(j)-v_L(j))+\Psi_{fb})}] \qquad (7) \\ & \times dx(j)\}. \end{aligned}$$

The total scattering from the fish is given as:

$$f_{bs}^{(tot)} = f_{bs}^{(sb)}, \qquad (ka < 0.15) \quad (8)$$

$$= f_{bs}^{(sb)} + f_{bs}^{(fb)}, \qquad (ka > 0.15) \quad (9)$$

where the choice of expressions using either Eq. (5) or (6) for $f_{bs}^{(sb)}$ is implicit in Eqs. (8) and (9) and depends on the particular value of $ka$.

## 2. FMM

The Fourier matching method (FMM) used herein to describe the scattering by the swimbladder involves the use of a two-dimensional conformal mapping approach to describe scattering by axisymmetric, irregular, finite-length bodies of revolution (Reeder and Stanton, submitted). The model conformally maps the coordinate variables of the original coordinate system to a new orthogonal coordinate system in which the new radial coordinate being a constant exactly coincides with the scatterer surface. The solutions to the transformed Helmholtz equation are a general solution for the total pressure in the case of far-field scattering by a finite body of revolution. This model has been shown to be very accurate in the prediction of scattering by smooth, symmetric bodies for a wide range of frequencies (resonance in the Rayleigh region through the geometric scattering region), scattering angles (monostatic and bistatic), aspect ratios and boundary conditions. Reasonable agreement has also been demonstrated for irregular, realistic shapes when compared to the Kirchhoff approximation (Reeder and Stanton, submitted).

Using a conformal mapping function of the form:

$$G(\rho) = c_{-1}e^{\rho} + \sum_{n=0}^{\infty} c_n e^{-n\rho}, \tag{10}$$

where $c_n$ are the conformal mapping coefficients determined by solving a system of non-linear constraints using the Newton-Raphson method, the coordinate system is mapped to a new, orthogonal coordinate system in which the constant radial coordinate exactly coincides with the scatterer surface (in this case, the swimbladder outer boundary). The scattering amplitude in

the new coordinate system is:

$$f = \sum_{n=-\infty}^{\infty} \sum_{m=-\infty}^{\infty} b_{nm} i^{-n-1} P_n^m \left( \frac{g(u,w)}{r(u,w)} \right) e^{imv}, \tag{11}$$

where $b_{nm}$ are the far-field scattering coefficients that depend on the shape and material properties of the scatterer, $P_n^m$ is the associated Legendre function, $r(u,w)$ is the new radial coordinate, and $g(u,w)$ is a function of the new system. The far-field scattering coefficients, $b_{nm}$, are determined after solving the transformed Helmholtz equation and satisfying the boundary conditions at the surface of the scatterer. Details and definitions of the parameters are in Reeder and Stanton (submitted). The FMM results presented here are based upon the scattering by the swimbladder alone—they do not include the computation of scattering from the fish body. As a consequence, the FMM will expectedly underpredict the scattering. Another approximation, as with the Kirchhoff method above, is the modeling of the surface as being constructed from a series of circular slices. The slices with the FMM are coaxial.

## III. EXPERIMENTAL METHODS

Seventeen adult alewife fish were used in the acoustic backscattering measurements during the month of May, 2000. The morphology of the fish was characterized through a combination of dissection and three x-ray technologies. The scattering measurements were performed on individual fish secured in a tether in a laboratory tank.

### A. Animals

Alewife were chosen because they are readily caught and are similar to the important fish, Atlantic herring (*Clupea harengus*), in their body size, shape and swimbladder construction

(Fig. 2). Both alewife and Atlantic herring expand and contract their swimbladders primarily by transferring air via a pneumatic duct between their esophagus and swimbladder. Other methods of maintaining buoyancy include diffusion and secretion of gases via a network of blood vessels and gas glands in contact with the swimbladder.

The fish were collected as they were migrating upstream to spawn in the freshwater ponds of Cape Cod, MA. The standard (caudal) lengths (measured from the nose to the end of the flesh near the tail) of these fish were quite uniform, averaging 22 cm. Their body weights averaged 144 grams. Since these fish were ready to spawn, their gonads were enlarged (Fig. 2b). The males' gonads were approximately 10% of their body weight, while the females' gonads equaled as much as 15% of their body weight. The animals' physical dimensions and weights are summarized in Table 1.

### B. Morphometry of animal shapes: PCX and CT scans

In addition to visual inspection of the fish (both whole and in dissected form), the morphology was investigated through quantitative use of various x-ray technologies—traditional x-rays, phase-contrast x-rays (PCX) and computerized tomography (CT) scans. After the acoustic measurements were recorded, traditional x-rays (Fig. 2d) of the fish were performed at the Falmouth Animal Hospital in N. Falmouth, Massachusetts. These x-ray images, measured in both the dorsal/ventral and lateral planes, were later used to generate hand-traced digitized objects of the swimbladder and fish body for use in the KRM model. Traditional x-rays are gray-scale images produced on a film that is sensitive to the amplitude of energy absorbed by an object. However, x-rays change not only in amplitude, but also in phase as the material distorts the wave as it passes through the material. Traditional x-ray imagery ignores this distortion, yet

the newly developed PCX process captures these phase changes, resulting in a high-resolution image that contains much finer detail than traditional x-ray images (Wilkins, 1996; Davis and Stevenson, 1996; Gureyev *et al.*, 2000). PCX imaging, performed on an alewife at the Commonwealth Scientific and Industrial Research Organisation (CSIRO) in Melbourne, Australia, is sensitive to, and illustrates well, the small-scale anatomical features of alewife such as fins, ribs, striations in muscle tissue, gills and weakly scattering soft tissue (Fig. 3). Such high-resolution imagery dramatically aids the determination of the scattering features in fish.

Additionally, high-resolution computerized tomography (CT) scans were performed on an alewife at the Falmouth Hospital in Falmouth, Massachusetts (Fig. 4). The CT scans are an efficient and non-invasive method of producing high-resolution three-dimensional images of fish. This method is in contrast to the direct, but time-consuming, method of microtoming (Foote, 1985; Ona, 1990). The images produced by the scans were used to generate a three-dimensional digital object of the swimbladder to be incorporated into the FMM scattering model. These data especially helped in determining the radius of curvature of each cross-sectional slice—an important element of the model. The alewife was scanned along the longitudinal axis of the animal, producing 112 images 2 mm apart. "Slices" of the fish were created to examine the morphology of the animal in each cross section. The original CT images contained 500 x 900 pixels, but were then cropped (referenced to a common pixel to maintain accurate physical proportions) for ease of numerical manipulation. The CT images were then converted to a three-dimensional binary matrix, each element of which contained a "1" for each element of the original matrix whose value was above a certain threshold. Using this approach, a three-dimensional digital object of the fish was produced (Fig. 5, upper panel). A wire-cage diagram

was then created of the fish body to better illustrate the exact physical morphology of the fish and its swimbladder (Fig. 5, lower panel). Coordinate points were then extracted from the top, bottom and side boundaries of the digital object of the swimbladder.

Each of the three boundaries was rotated about an axis to form three bodies of revolution to separately model the scattering in the two planes—dorsal/ventral and lateral. There are two models associated with the dorsal/ventral plane—one for the dorsal aspect and the other for the ventral aspect. For the ventral and lateral models, the axis of rotation was simply the straight line between the two outer-most points at the (front and back) ends of the swimbladder. However, given the straight profile of the dorsal side of the swimbladder (Fig. 5, lower panel), this approach produced unrealistically small cross-sectional slices which significantly underpredicted the scattering. This difficulty was remedied by choosing an axis that passes through the center of the middle section of the swimbladder, resulting in realistic values of cross-sectional radii. Once the surfaces were constructed, the points were used by the FMM to conformally map each of the three swimbladder shapes into a new coordinate system in which the new radial coordinate exactly matches the surface of the body.

### C. Acoustic data acquisition

The acoustic backscattering measurements were conducted in a large freshwater tank at Benthos, Inc. in North Falmouth, MA (Fig. 6). The experimental setup, similar in concept to that described in Stanton *et al.* (2000), included the use of a power amplifier, signal generator, a pair of transducers, pre-amplifier, band-pass filter, oscilloscope and personal computer. All of these components, except for these particular transducers, were used in the experiment described in Stanton *et al.* (2000). During the measurements, the individual fish were secured in an acousti-

cally transparent harness in the center of the acoustic beam and rotated. Although all animals were alive and in good condition at the beginning of each measurement, some died part-way into the measurement. The data presented here are from nine data sets on three animals (15, 17 and 26), all of which remained alive for the entire measurement.

A pair of Reson TC2116 broadband acoustic transducers was mounted horizontally in the tank facing the fish in the tethering system, the center of which was attached to a computer-controlled stepper motor which rotated the assembly in $1^0$ increments through two full rotations (720 pings per data set). The two transducers were identical and closely spaced, one used as the transmitter and one as the receiver, approximating a monostatic configuration. The use of two transducers allows closer scattering ranges, minimizes the effect of transmitter ringing and makes the system easier to calibrate. The fish were insonified with a shaped chirp signal with a usable frequency spectrum ranging from 40kHz to 95kHz (Fig. 7). The transmitted signal was shaped to make the composite response of the transducer pair approximately uniform over the usable bandwidth. The transmitted voltage time series, $v_{bs}^T(t)$, and the received voltage time series (the backscattered return echo from the animal), $v_{bs}^R(t)$, were stored on a personal computer for later analysis. The beamwidth of each transducer at the intermediate frequencies was approximately 14 degrees.

The tethering system consisted of a specially designed, hand-made harness (Fig. 6 inset) made of 4 lb. test fishing line suspended in the tank by six lines to a frame mounted just above the surface of the water and by six lines to a frame near the bottom of the tank. The harness was designed to hold the fish in the center of the acoustic beam and at a constant range ($r_{bs} = 4.3$ m) from the transducers as the fish was rotated. The harness uses the least amount of material

possible in order to be acoustically transparent. It was also designed to provide just enough restriction to prevent escape while allowing the fish to move as freely as possible to minimize stress. The harness has six longitudinal lines, one on the top, one on the bottom and two along each side. The vertical members of the harness are spaced more closely together near the head of the fish to prevent escape, and spaced farther apart toward the rear of the fish to allow for freedom of movement. The vertical members near the gills are spaced so as not to restrict the gills. The harness has a cinch at the front that is tightened before the fish is slipped head-first into the harness from the back. Once the experiment is complete, the cinch is loosened and the fish can be removed by slipping it forward through the front of the harness, avoiding damage to the fins and scales of the fish. The lines to each of the points on the top and bottom frames can be used to adjust the precise position of the harness in the tank. The bottom frame is suspended just above the bottom of the tank by the six bottom lines so that it is outside of the acoustic beam but does not drag on the bottom of the tank.

Before each fish was placed in the tether, much attention was given to ensuring that the harness was located in the center of the acoustic beam and was free of bubbles. Underwater lasers were mounted and aligned on the bottom of the transducers to aid in the alignment of the transducers (Fig. 6). Due to the relatively large distances involved, these lasers proved to be indispensable in the process of alignment. The tether system was adjusted so that when the fish was placed in the harness for measurement, the system would pivot about the approximate center of its swimbladder. To eliminate bubbles coalescing on the harness, all of the lines on the tethering system were thoroughly wetted and rubbed with a soap solution prior to measurement. This process was done each time the tethering system was taken out of the water for any reason.

Additionally, a small amount of soap was applied to each transducer face before calibration and measurement to ensure good contact with the water and to minimize adherence of bubbles that could contaminate the acoustic signals.

The background reverberation of the tank was taken into account for the scattering measurements. The background reverberation signals (with no fish in the tank) were first summed over hundreds of pings and the resultant (unwanted) coherent echo was then stored in the digital oscilloscope. While collecting backscattering signals from the fish, the stored background reverberation signal was subtracted from the echo in real time by the oscilloscope. The difference signal that was stored, $v_{bs}^{R}(t)$, during the experiment consisted of the echo from the fish and random noise of the entire system.

The system was carefully calibrated prior to each set of backscattering measurements following the pseudo-self-reciprocity calibration procedure referred to by Urick (1983) and outlined in detail by Stanton *et al.* (1998a). The system was calibrated by mounting the transducers such that they faced each other and were separated by a range of $r_{cal} = 4.1$ m. The time series of the shaped, chirp transmitted calibration ($v_{cal}^{T}(t)$) voltage and the average of hundreds of received ($v_{cal}^{R}(t)$) calibration voltages were stored on a computer and used later in order to calculate fish target strengths. The received calibration signal was also used in the pulse compression analysis discussed in Section II.

Taking into account the calibration information, the magnitude of the scattering amplitude of the fish was computed for each ping:

$$|f_{bs}| = \frac{V_{bs}^{R}}{V_{cal}^{R}} \frac{V_{cal}^{T}}{V_{bs}^{T}} \frac{r_{bs}^{2}}{r_{cal}}, \tag{12}$$

where $V_{bs}^R$, $V_{bs}^T$, $V_{cal}^R$ and $V_{cal}^T$ are the absolute values of the Fourier transforms of the band-pass filtered voltage time series $v_{bs}^R$, $v_{bs}^T$, $v_{cal}^R$ and $v_{cal}^T$ (Fig. 7).

## IV. EXPERIMENTAL RESULTS

The broadband signals have been analyzed in both the frequency and time domains. The orientation dependence of the scattering has been examined for each Fourier component of the signal, and the spectral and temporal patterns have been examined for every orientation angle. Given the great difference in shape of the swimbladder in the dorsal/ventral and lateral planes, the results from these different planes are analyzed.

### A. Spectral domain

Acoustic backscattering strength was observed to be strongly dependent upon acoustic frequency and animal orientation (Figs. 8 - 11). These relationships are demonstrated in both planes of scattering—dorsal/ventral and lateral. Generally, the target strength is maximum near normal incidence. Also, at fixed angles of orientation, the target strength varies with frequency, represented by a series of peaks and nulls (Fig. 11).

The beamwidth of the main scattering lobes from the fish generally becomes more narrow with increasing frequency (Figs. 8 - 10). Ventral aspect scattering is generally less directional than corresponding dorsal aspects (Figs. 9 and 10).

### B. Time domain

The compressed pulse output (CPO) shows separation of the echo into multiple highlights, apparently due to different dominant scattering features in the fish (Figs. 12 - 14). In order to analyze this in terms of the scattering, time of arrival has been converted into separation

distances along the length of the fish. The overall separation and structure of the highlights in the CPO are a strong function of orientation angle. At normal incidence, there is generally a single, dominant peak. At oblique angles of incidence, multiple significant peaks are present in the received signal. The separation between the first and last arrivals tends to increase for angles away from normal incidence.

The concept of partial wave target strength (PWTS) was introduced by Chu and Stanton (1998) to characterize the contributions by various individual highlights or partial waves that make up the total backscattered signal from the animal. PWTS is achieved by partitioning, or time-gating, the CPO to isolate scattering highlights of interest. The spectral characteristics of the PWTS features of these echoes are significantly different than that of the total signal (Figs. 15 and 16).

## V. MODELING AND COMPARISON WITH DATA

### A. Relating scattering features to fish anatomy

The dependencies of acoustic backscattering strength of the alewife on orientation, frequency and morphology are clearly seen in the data. The narrow width of the main lobes indicated in Fig. 8 correlates to scattering from the relatively long, narrow swimbladder and body. The difference between dorsal and ventral scattering directivity in Figs. 9 and 10 is also consistent with an elongated shape that also possesses a difference in the curvature between the two sides (i.e., as illustrated in Figs. 2d, 3 and 5, the ventral side of the swimbladder is more rounded in the length-wise direction than the dorsal side). The pattern of peaks and nulls in Fig. 11 is consistent with constructive and destructive interference between multiple rays scattering from

different parts of the body. The rays add constructively or destructively depending upon the location of the part of the body from which it is scattered, the frequency of the signal, and the angle of orientation in relation to the source/receiver transducer pair. Maximum target strength occurs near normal incidence, as these multiple arrivals are in phase (or nearly so) and add coherently to the total target strength. As the orientation moves away from normal incidence, the arrivals become well out of phase and add destructively at certain frequencies as evidenced by the one null and two broad peaks at near normal incidence. At more oblique angles, the peaks and nulls are more closely spaced as constructive and destructive interferences occur at more frequencies within the band.

Through pulse compression processing, the individual arrivals from different parts of the body (which apparently cause the interference patterns in the spectral plots) are resolved, resulting in several significant scattering features being extracted from the received signal (Fig. 12). The separation of the peaks correlates with the physical separation between the skull and swimbladder of the alewife used in the experiment.

The separation in time of the arrivals from individual scattering features in the fish as it rotated in the acoustic beam is illustrated in Fig. 13. At tail-on orientation, the scattering features nearest the tail scatter the incident wave first, followed by scattering from other features as the incident wave travels from tail to head. As the orientation moves toward normal incidence, the time separation between the partial waves decreases as the physical separation of the scattering features along the line between the transducers and fish decreases. As the orientation moves toward head-on, the time separation increases again. The temporal distribution of the arrivals from different significant scatterers in the fish in Fig. 13 is apparent and is consistent

with the physical separation of the scattering features in the fish. In order to further elucidate the contributions of individual scatterers in the fish as a function of orientation, temporal separation is converted to spatial separation along the length-wise axis of the fish (Fig. 14). The arrival nearest to the tail and apparently from the swimbladder, is generally the most significant contributor to the overall scattering throughout the 90 degree rotation. The scattering near the end of the time series, apparently from the skull, is initially shadowed by the body of the fish and cannot be detected acoustically. As the fish is rotated toward normal incidence, the skull exits the acoustic shadow, and the amplitude of the arrival from the skull increases. The arrivals between the skull and swimbladder demonstrate complicated variable scattering mechanisms that are orientation dependent. The two significant scatterers within the fish nearest the head and tail are separated by approximately 12 cm, correlating with the anatomical dimensions of the fish.

Partial wave target strength (PWTS) makes more evident the characteristics of selected arrivals in the backscattered signal and their interactions (Fig. 15). These constructive and destructive interferences vary as the animal's orientation changes according to the separation (relative to the transducers) of the scattering features with respect to the wavelength of the sound. At normal incidence, the multiple arrivals are in phase (or nearly so) and add coherently, resulting in a relatively flat response over the band. As the orientation moves away from normal incidence, the arrivals add less coherently, causing the individual waves to add destructively at certain frequencies, which results in a series of peaks and nulls in the target strength over the frequency band. If the multiple arrivals are analyzed separately, the interference mechanism can be further elucidated (Fig. 16). The partial wave target strengths of the individual first and

second major arrivals at oblique angles exhibit smooth and relatively flatter responses than that of a combination of the two arrivals. This further illustrates the hypothesis that these resolved echoes are due to multiple singular scattering features which make significant contributions to the overall scattering.

## B. Modeling the scattering

For all animals, it has been demonstrated experimentally that the acoustic backscattering is strongly dependent upon morphology, angle of orientation and frequency. In an effort to quantify these dependencies, the FMM and KRM models were used for predictions of target strength vs. angle to compare to the acoustic measurements of the alewife. Although, as shown above, there are several scattering features in the fish, the FMM predictions are based upon scattering from high resolution representations of the swimbladder alone, which is the dominant scatterer near normal incidence, modeled with soft, or pressure-release, boundary conditions. The KRM results are based upon the coherent addition of the scattering from the swimbladder with soft boundary conditions and the scattering from the fish body with fluid boundary conditions.

Experimental data and accompanying model calculations are presented for two different fish (#15 and #17) at dorsal and ventral aspects at three different frequencies (Figs. 17 and 18). There is generally reasonable agreement between the models and data in the general structure of the target strength as a function of orientation. Both models and data demonstrate well the more narrow acoustic beampattern at dorsal aspect compared to that of the ventral aspect, which is consistent with morphology. Also consistent with morphology is the position of the center of the main lobe near normal incidence.

Both models compared best with the data in the main lobe of the scattering (i.e., near normal

incidence) for the case of dorsal aspect (Figs. 17 and 18, left columns). In those cases, the KRM predictions are either very close to the data or slightly underpredict. The FMM consistently underpredicts relative to the data by about 3-5 dB. Underpredictions in both cases can be explained, at least in part, by the fact that only the swimbladder is taken into account with the FMM and only the swimbladder plus body with the KRM. Also, as discussed earlier, although the swimbladder and body shapes were modeled at very high resolution, the process still involved a series of approximations, which is a source of error in the modeling both for dorsal and ventral aspects.

For angles well off normal incidence (dorsal aspect case), the KRM consistently underpredicts the scattering, sometimes by up to 15 dB below the measurements. In contrast, the FMM is much closer to the data and, for some ranges of angles (such as within 20 degrees of the main lobe for dorsal aspect), the FMM predictions are within the range of values of data collected (Figs. 17 and 18, left columns, second panel from bottom).

These differences between KRM and FMM predictions for angles well off normal incidence are expected. The KRM, which is based on the Kirchhoff model at these frequencies, is inherently inaccurate at angles well off normal incidence, and expectedly underpredicts the scattering levels in that region. The FMM, as demonstrated in Reeder and Stanton (submitted), is valid for all angles of orientation. Deviations between the FMM predictions and data in this region are expected to be due to the modeling of the shape of the swimbladder (scattering well off normal incidence is especially sensitive to precise shape of target) and exclusion of other parts of the fish anatomy.

For the cases involving ventral aspect (Figs. 17 and 18, right columns), both models under-

predicted near-normal incidence scattering by a larger degree than with the dorsal aspect cases. For angles well off normal incidence, the FMM predictions were generally closer to the data than those from the KRM model (similar to the dorsal aspect cases). The biggest difference between the dorsal and ventral aspect cases is the fact that the large gonads are directly beneath the swimbladder (Fig. 2b). One plausible explanation for the larger discrepancy between predictions and data in the ventral aspect case may be the added scattering by the gonad.

## VI. DISCUSSION AND CONCLUSIONS

There are several important advancements made in this study involving use of advanced imagery of fish morphology, broadband acoustical measurements, and the modeling: 1) The CT-scan imagery proved to be a useful tool in synoptically and non-invasively mapping major morphological features of the fish. As suggested above, this approach appears to be a viable alternative to, or at least a method complementary to, the tedious process of microtoming. In addition to the insight that this method and the phase-contrast x-ray provided in qualitatively understanding the morphology of the fish without dissection, the CT-scan was useful in the modeling. The digitally constructed 3-D image of the swimbladder was used in this case to provide the lengthwise profile of the swimbladder shape for the FMM model as well as to aid in the determination of the location of the axis of rotation for that model. 2) The broadband measurements provided information across a continuous range of frequencies (simultaneously) that was useful in the modeling. Furthermore, through pulse compression of the broadband echoes, the data provided insight into the dominant scattering mechanisms. For angles well off normal incidence, it provided quantitative data on the relative contribution of the various scattering features of the fish. 3) The comparison of model predictions with the data provided further validation of the

range of accuracy of the KRM model as well as providing a first test of the applicability of the FMM model with the fish scattering problem. Clearly, the Kirchhoff-based KRM model is valid for angles of orientation near normal incidence. However, well off normal incidence, the KRM approach greatly underpredicts the scattering. The utility of the FMM approach in this latter case is apparent, consistent with the fact that the model is valid for all angles of orientation, at least with objects with simple shapes (Reeder and Stanton, submitted).

The above advances yield potential for future advances. For example, as the push for advanced, reliable, 3-D models of acoustic scattering by fish continues, there is a corresponding need for high resolution 3-D information on the morphology. The CT scan imagery was demonstrated here to provide valuable 3-D morphological information for the fish problem, as well as to be collected rapidly, as it already has for the zooplankton acoustics problem (Lavery *et al.*, 2002). The utility of broadband acoustics has already been demonstrated in the ocean where incoherent processing of the broadband echoes has allowed for discrimination of fish species (Simmons *et al.*, 1996; Zakharia *et al.*, 1996). Through (coherent) pulse compression processing of the broadband echoes, the scattering (at least in the laboratory) can be investigated at high resolution and, as a result, scattering models can be further advanced by allowing inclusion of parts of the anatomy beyond the swimbladder. This advancement would be especially important for angles well off normal incidence where the contribution of the swimbladder does not necessarily dominate the scattering. Finally, advanced scattering models are needed to be accurate over a wider range of conditions. New models such as the FMM and BEM (Foote and Francis, 2002) have potential for modeling the scattering over a much larger range of orientation angles and frequencies, including near the resonance frequency of the swimbladder. Carefully taking into account high resolution

morphology as well as comparisons with data over a wide range of frequencies and orientations will help further advance the development of new models.

## ACKNOWLEDGMENTS

The authors would like to thank Falmouth Hospital for performing the CT scans of the alewife, Falmouth Animal Hospital for the use of their x-ray machine, and Benthos, Inc. for the use of their test tank for the acoustic measurement portion of the study. Andrew Stevenson, D. Gao and Steve Wilkins at Australia's Commonwealth Scientific and Industrial Research Organisation (CSIRO) have been very generous in their PCX imaging of the fish. The help of Hanu Singh, Andone Lavery and the Graphics Department at the Woods Hole Oceanographic Institution with image processing was much appreciated. This work was supported by the U.S. Navy, the U.S. Office of Naval Research, the National Oceanographic and Atmospheric Administration, and the Massachusetts Institute of Technology/Woods Hole Oceanographic Institution Joint Program in Oceanographic Engineering. This is Woods Hole Oceanographic Institution Contribution Number XXXXX.

## REFERENCES


Andreyeva, I.B. (1964) "Scattering of sound by air bladders of fish in deep sound-scattering ocean layers," Sov-Phys-Acoust., 10:17-20.

Benoit-Bird, K.J., and Au, W. W. L. (2001). "Target strength measurements of Hawaiian mesopelagic boundary community animals," J. Acoust. Soc. Am., 110:812-819.

Chu, D., and Stanton, T.K. (1998) "Application of pulse compression techniques to broadband acoustic scattering by live individual zooplankton," J. Acoust. Soc. Am., 104:39-55.

Clay, C.S., and Heist, B.G. (1984) "Acoustic scattering by fish-acoustic models and a 2-parameter fit," J. Acoust. Soc. Am., 75:1077-1083.

Clay, C.S. (1991) "Low-resolution acoustic scattering models: Fluid-filled cylinders and fish with swimbladders," J. Acoust. Soc. Am., 89:2168-2179.

Clay, C.S., and Horne, J.K. (1994) "Acoustic models of fish: The Atlantic cod (*Gadus morhua*)," J. Acoust. Soc. Am., 96:1661-1668.

Davis, T.J., and Stevenson, A.W. (1996) "Direct measure of the phase shift of an x-ray beam," J. Opt. Soc. Am., 13: 1193-1198.

Diercks, K.J., and Goldsberry, T.G. (1970) "Target strength of a single fish," J. Acoust. Soc. Am., 48:415-416.

Do, M.A., and Surti, A.M. (1990) "Estimation of dorsal aspect target strength of deep-water fish using a simple model of swimbladder back scattering," J. Acoust. Soc. Am., 87:1588-1596.

Feuillade, C., and Nero, R.W. (1998) "A viscous-elastic swimbladder model of describing enhanced-frequency resonance scattering from fish," J. Acoust. Soc. Am., 103:3245-3255.

Foote, K.G. (1985) "Rather-high-frequency sound scattering by swimbladdered fish," J. Acoust. Soc. Am., 78:688-700.

Foote, K.G. (1987) "Fish target strengths for use in echo integrator surveys," J. Acoust. Soc. Am., 82:981-987.

Foote, K.G. (1997) "Target strength of fish," In *Encyclopedia of Acoustics* (Ed. by Malcolm J. Crocker, John Wiley and Sons, New York).

Foote, K.G. (2001) "Acoustic scattering by marine organisms," In *Encyclopedia of Ocean Sciences* (Ed. by J.H. Steele, K.K. Turekian and S.A. Thorpe; Academic Press, London).

Foote, K. G., and Francis, D. T. I. (2002) "Comparing Kirchhoff-approximation and boundary-element models for computing gadoid target strengths," J. Acoust. Soc. Am., 111:1644-1654.

Furusawa, M. (1988) "Prolate spheroidal models for predicting general trends of fish target strength," J. Acoust. Soc. Jpn. (E), 9:13-24.

Gunderson, D.R. (1993) *Surveys of Fisheries Resources* (John Wiley and Sons, New York).

Gureyev, T.E., Stevenson, A.W., Paganin, D., Mayo, S.C., Pogany, A., Gao, D., and Wilkins, S.W. (2000) "Quantitative methods in phase-contrast x-ray imaging," J. of Dig. Imaging, 13: 121-126.

Haslett, R.W.G. (1962) "Determination of the acoustic scatter patterns and cross sections of fish models and ellipsoids," Br. J. Appl. Phys., 13:611-620.

Haslett, R.W.G. (1969) "The target strengths of fish," J. Sound Vib., 9:181-191.

Horne, J.K., and Jech, J.M. (1999) "Multi-frequency estimates of fish abundance: constraints of rather high frequencies," ICES J. Mar. Sci., 56:184-199.

Jones, F.R.H., and Pearce, G. (1958) "Acoustic reflexion experiments with perch (*Perca fluviatilis Linn.*) to determine the proportion of the echo returned by the swimbladder," J. Exp. Biol., 35:437-450.

Kjaergaard, L., Bjorno, L., Kirkegaard, E., and Lassen, H. (1990) "Broadband analysis of acoustical scattering by individual fish," Rapp. P.-v. Reun. Cons. Int. Explor. Mer., 189:370-380.

Lavery, A.C., Stanton, T.K., McGehee, D.E., and Chu, D. (2002) "Three-dimensional modeling of acoustic backscattering from fluid-like zooplankton," J. Acoust. Soc. Am., 111:1197-1210.

Love, R.H. (1969) "Maximum side-aspect target strength of an individual fish," J. Acoust. Soc. Am., 46:746-752.

Love, R.H. (1970) "Dorsal-aspect target strength of an individual fish," J. Acoust. Soc. Am., 49:816-823.

Love, R.H. (1971) "Measurements of fish target strength: A review," Fishery Bulletin, 69:703-715.

Love, R.H. (1977) "Target strength of an individual fish at any aspect," J. Acoust. Soc. Am., 62:1397-1403.

Love, R.H. (1978) "Resonant acoustic scattering by swimbladder-bearing fish," J. Acoust. Soc. Am., 64:571-580.

Medwin, H., and Clay, C.S. (1998) *Fundamentals of Acoustical Oceanography* (Academic Press, Boston).

Midttun, L. (1984) "Fish and other organisms as acoustic targets," Rapp. P.-v. Reun. Cons. Int. Explor. Mer., 184:25-33.

Miyanohana, Y., Ishii, K., and Furusawa, M. (1990) "Measurements and analyses of dorsal-aspect target strength of six species of fish at four frequencies," Rapp. P.-v. Reun. Cons. Int. Explor. Mer., 189:317-324.

Nakken, O., and Olsen, K. (1977) "Target strength measurements of fish," Rapp. P.-v. Reun. Cons. Int. Explor. Mer., 170:52-69.

Nash, D.M., Sun, Y., and Clay,C.S. (1987) "High resolution acoustic structure of fish," J. Cons. int. Explor. Mer., 43:23-31.

Ona, E. (1990) "Physiological factors causing natural variations in acoustic target strength of fish, " J. Mar. Biol. Assoc. U.K., 70:107-127.

Reeder, D.B. and Stanton, T.K. (submitted) "Acoustic scattering by axisymmetric finite bodies: an extension of a 2-dimensional conformal mapping method," J. Acoust. Soc. Am.

Simmonds, J.E., Armstrong, F., and Copland, P.J. (1996) "Species identification using wideband backscatter with neural network and discriminant analysis," ICES J. Mar. Sci., 53:189-195.

Stanton, T.K. (1988) "Sound scattering by cylinders of finite length. I. Fluid cylinders," J. Acoust. Soc. Am., 83:55-63.

Stanton, T.K. (1989) "Sound scattering by cylinders of finite length. III. Deformed cylinders," J. Acoust. Soc. Am., 86:691-705.

Stanton, T.K., Wiebe, P.H., Chu, D., Benfield, M.C., Scanlon, L., Martin, L., and Eastwood, R.L. (1994) "On acoustic estimates of zooplankton biomass," ICES J. Mar. Sci., 51:505-512.

Stanton, T.K., Chu, D., Wiebe, P.H., Martin, L.V., and Eastwood, R.L. (1998a) "Sound scattering by several zooplankton groups. I. Experimental determination of dominant scattering mechanisms," J. Acoust. Soc. Am., 103:225-235.

Stanton, T.K., Chu, D., Wiebe, P.H. (1998b) "Sound scattering by several zooplankton groups: II. Scattering Models," J. Acoust. Soc. Am., 103:236-253.

Stanton, T.K., Chu, D., Wiebe, P.H., Eastwood, R.L., and Warren, J.D. (2000) "Acoustic scattering by benthic and pelagic shelled animals," J. Acoust. Soc. Am., 108:535-550.

Stevenson (2002) Personal communication.

Turin, G.L. (1960) "An introduction to matched filters," IRE Trans. Info. Thy., IT-6:311-329.

Urick, R.J. (1983) *Principles of underwater sound* (Peninsula Publishing).

Weston, D.E. (1967) "Sound propagation in the presence of bladder fish," *Underwater Acoustics*, Ed. by V.M. Albers (Plenum Press, New York).

Wilkens, S.W., Gureyev, T.E., Gao, D., Pogany, A., and Stevenson, A.W. (1996) "Phase-contrast imaging using polychromatic hard x-rays," Nature, 384:335-338.

Ye, Z., and Farmer, D.M. (1994) "Acoustic scattering from swim-bladder fish at low frequencies," J. Acoust. Soc. Am., 96:951-956.

Ye, Z. (1996) "Acoustic scattering from fish swimbladders," J. Acoust. Soc. Am., 99:785-792.

Zakharia, M.E., Magand, F., Hetroit, F., and Diner, N. (1996) "Wideband sounder for fish species identification at sea," ICES J. Mar. Sci., 53:203-208.

Figure Captions

Fig. 1: Relative acoustic pressure as recorded along the length for a largemouth bass showing relative scattering contributions by the whole fish, head, vertebral column and swimbladder. This qualitative illustration of the dependence of fish target strength on changes in morphology was generated through the use of a focused array transducer system that scanned the length of the object at 220 kHz in the near-field. Adapted from Nash *et al.* (1987).

Fig. 2: Images of Alewife #18 used in the acoustic scattering experiments: (a) whole fish, (b) dissected fish showing enlarged gonads (large organ immediately below swimbladder), (c) dissected fish with gonads removed to expose the swimbladder and (d) traditional x-ray of whole fish showing (dark) outline of swimbladder. The fish were collected as they swam upstream to spawn in the freshwater ponds of Cape Cod, Massachusetts; consequently, their gonads were enlarged as seen in the images. All of the fish were adults with an average caudal length of 22 cm and an average body weight of 144 grams.

Fig. 3: Phase-contrast x-ray (PCX) of Alewife #25. Imaging was performed at the Commonwealth Scientific and Industrial Research Organisation (CSIRO) in Melbourne, Australia. The PCX process is an extremely high-resolution imaging technique which is sensitive to weakly scattering body tissue. Slight morphological details can be detected,

such as the gills, fins, ribs, striations in the muscle tissue, gonads and gut (Stevenson (2002)).

Fig. 4: High-resolution computerized tomography (CT) scan images of Alewife #3 (not listed on Table 1) with their placement indicated along the fish body. The black areas within the cross-sectional slices include the swimbladder and gas-inclusions in the gut, which is connected to the esophagus near the head. The vertebral column and muscle tissue can also be seen in the images.

Fig. 5: Three-dimensional digital objects generated from CT scan imagery: whole fish (upper panel) and wirecage diagram of fish body with swimbladder object inside (lower panel). The 112 images generated during the CT scan were processed by a digital image processing algorithm to generate the exact shapes to incorporate into the FMM for scattering predictions. The swimbladder image from the CT scan was quite distinct, and there were no issues in detecting and digitizing its outer boundary.

Fig. 6: Schematic of the laboratory system used for measuring acoustic backscattering by live, individual fish as a function of angle of orientation and frequency: tank, transducers, lasers used for alignment, stepper motor to rotate the animal in the acoustic beam and acoustically transparent tether system. The photograph of the harness, shown in the inset, was enhanced so the thin monofilament could be illustrated.

Fig. 7: Broadband chirp signals: time series of voltage signal as applied to the transmitting transducer and used during both the scattering experiment and calibration; time series of calibration signal as measured at the output of receiving transducer; frequency spectrum of received calibration signal; and envelope of auto-correlation function (compressed pulse) of the received calibration signal which corresponds to matched filter output. The transmitted signal was shaped to flatten the composite response of the transducer pair across the frequency band of 40-95kHz. The received calibration signal was stored for later use in the analysis to generate absolute target strengths on a ping-by-ping basis. The normalized compressed pulse output has sidelobes which are numerical processing artifacts with maximum peaks of 0.365. These sidelobes can introduce spurious artificial echoes in the analysis which must be taken into account.

Fig. 8: Magnitude of backscattering amplitude as a function of angle as measured for Alewife 26 in the lateral plane at 50 kHz, 70 kHz and 95 kHz. Tail-on orientation corresponds to 0 degrees. Each plot is on a linear scale, normalized to unity and based on a one-ping recording for each one-degree increment of rotation.

Fig. 9: Target strength as a function of angle of orientation as measured for Alewife 15 in the dorsal/ventral plane at 60 kHz and 90 kHz. Zero degrees corresponds to normal incidence relative to the dorsal or ventral sides for the left and right panels, respectively. For a free-swimming horizontally oriented fish, $0^{\circ}$ dorsal and $0^{\circ}$ ventral angles would correspond to a downward- and upward-looking acoustic transducer, respectively.

Fig. 10: Target strength as a function of angle of orientation as measured for Alewife 17 in the dorsal/ventral plane at 60 kHz and 90 kHz. The plotting convention is the same as in Fig. 9.

Fig. 11: Target strength as a function of frequency in the lateral plane as measured for Alewife 15 at broadside, near broadside and oblique angles of incidence. In this case, the oblique angle was 30 degrees from end-on, or 60 degrees from normal incidence. The near normal incidence angle is 5 degrees off normal.

Fig. 12: Envelope of normalized compressed pulse output (CPO) for Alewife 15 at approximately 30 degrees from tail-on orientation in the lateral plane. The time delay on the horizontal axis has been converted to distance (*cm*) to represent the spatial separation between the scattering features of the fish, using the equation: separation = (time delay) $*c / (2\cos(\beta))$, where $\beta$ is the angle of orientation relative to the transducer beam (as per polar plot in Fig. 8), and $c$ is the speed of sound. The processing sidelobe is an artifact of the pulse compression process, as illustrated in Fig. 7; therefore, any peak significantly higher than the processing sidelobe level represents a physical arrival from the fish.

Fig. 13: Envelope of normalized CPO (contour plot) for Alewife 17 as a function of angle of orientation and time delay, depicting the changing CPO as the fish is rotated from tail-on through normal incidence to head-on orientation in the dorsal/ventral plane.

Each segment of the plot corresponding to each degree of rotation is the CPO from a single realization at that particular angle of orientation. At angles near end-on, the individual arrivals are spread out in time, whereas at angles near normal incidence, the individual rays return nearly simultaneously. Reduced echoes due to shadowing are evident for angles near end-on incidence toward the end of each time series.

Fig. 14: Envelope of normalized CPO ("waterfall plot") for Alewife 15 as a function of angle of orientation and time delay converted to distance (along fish), depicting the changing CPO as the fish is rotated from tail-on to broadside orientation in the lateral plane. This figure is similar to Fig. 13, except that the conversion of time delay to distance allows better visualization of the scattering features and their changes as a function of angle of orientation.

Fig. 15: Normalized CPO, target strength and partial wave target strength (PWTS) of Alewife 15 at three different orientations in the lateral plane. The plots on the right are TS (thin lines) computed from the whole time series and PWTS (thick lines) computed from the thick-lined (time-gated) portions of the time series on the left.

Fig. 16: Normalized CPO, target strength and partial wave target strength (PWTS) for Alewife 15 in the lateral plane. All three pairs of panels are for the same oblique angle of orientation, but represent processing of different segments of the CPO. The top pair of plots is identical to the bottom pair plots of Fig. 15 for reference, while the lower four panels illustrate the characteristics of the separate arrivals.

Fig. 17: FMM (solid lines), KRM (dashed lines) and acoustic scattering data (dots): Target strength as a function of angle of orientation for Alewife 15 in the dorsal/ventral plane at 45, 65 and 85 kHz (top six panels), and band-wide statistics of target strength as a function of angle of orientation (bottom four panels). The three frequencies in the top six panels are representative of the measurements and predictions across the 40-95 kHz frequency band. The average target strengths were computed by averaging the backscattering cross sections across the band before taking the logarithm. The shaded areas in the lower four panels depict the standard deviation about the averaged measured values within the band, and the solid lines depict the corresponding standard deviation about the averaged FMM and KRM predictions. The plotting convention is the same as Fig. 9. Portions of the FMM predictions for the ventral aspect are not shown due to numerical difficulties. The difficulties are due to the particularly irregular interface of the ventral side of the swimbladder.

Fig. 18: Comparison of model predictions with data for Alewife 17. The plotting convention is the same as Fig. 17.

Table 3-1. Dimensions, weights and use (yes/no) of acoustic, (traditional) x-ray and dissection techniques for each of the alewife used in the acoustic scattering measurements. Total length (TL) is the distance from the nose to the tip of the tail. Caudal (standard) length (CL) is the distance from the nose to the end of the flesh near the tail. PCX imaging was performed on Alewife #25. CT scans were performed on Alewife #3 (not listed).

| Animal Desig | Animal Tag # | Gender | TL (mm) | CL (mm) | Height (mm) | Width (mm) | Weight (g) | Acoustic:X-ray:Dissection |
|---|---|---|---|---|---|---|---|---|
| 10 | 152 | F | 259 | 215 | 59.7 | 25.2 | 159 | Yes:No:Yes |
| 11 | 153 | M | 255 | 217 | 52.4 | 21.3 | 120 | Yes:No:Yes |
| 12 | 154 | M | 255 | 225 | 54.3 | 23.8 | 133 | Yes:Yes:Yes |
| 13 | 155 | F | 268 | 225 | 60.8 | 27.3 | 172 | Yes:Yes:Yes |
| 14 | 156 | M | 258 | 220 | 59.0 | 26.0 | 151 | Yes:Yes:Yes |
| 15 | 157 | F | 256 | 216 | 54.7 | 23.0 | 135 | Yes:Yes:Yes |
| 16 | 158 | M | 260 | 220 | 62.8 | 25.8 | 168 | Yes:Yes:Yes |
| 17 | 159 | F | 244 | 215 | 59.4 | 22.8 | 120 | Yes:Yes:Yes |
| 18 | 160 | M | 241 | 200 | 59.7 | 23.7 | 121 | Yes:Yes:Yes |
| 19 | 161 | M | 257 | 217 | 56.7 | 24.5 | 141 | Yes:Yes:Yes |
| 20 | 162 | F | 259 | 216 | 63.5 | 26.1 | 165 | Yes:Yes:Yes |
| 21 | 163 | M | 254 | 217 | 59.6 | 24.0 | 147 | Yes:Yes:Yes |
| 22 | 164 | * | 254 | 223 | 56.6 | 24.7 | 148 | Yes:Yes:No |
| 23 | 165 | F | 277 | 235 | 56.4 | 23.3 | 150 | Yes:Yes:Yes |
| 24 | 166 | F | 255 | 217 | 57.0 | 23.8 | 139 | Yes:Yes:Yes |
| 25 | 167 | * | 250 | 213 | 50.9 | 22.2 | 116 | Yes:Yes:No |
| 26 | 168 | * | 265 | 225 | 56.5 | 26.0 | 157 | Yes:Yes:No |

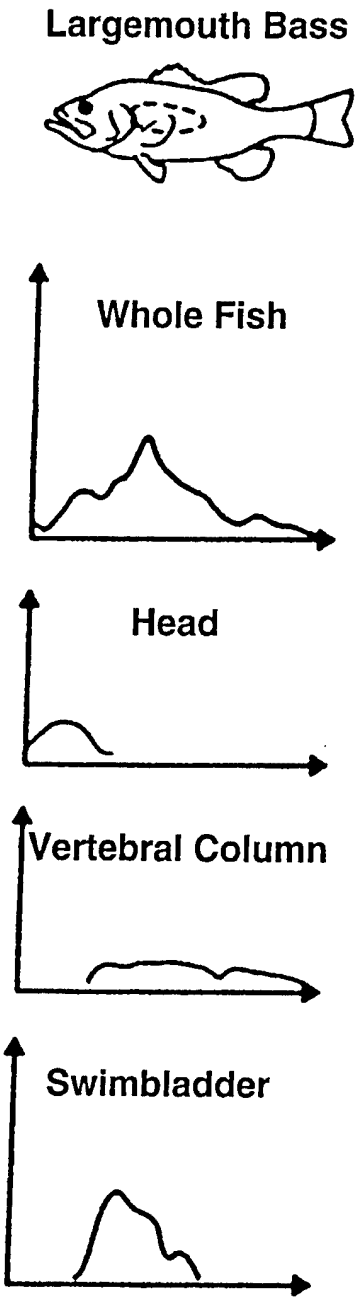
Largemouth Bass
Whole Fish
Head
Vertebral Column
Swimbladder

Fig 1

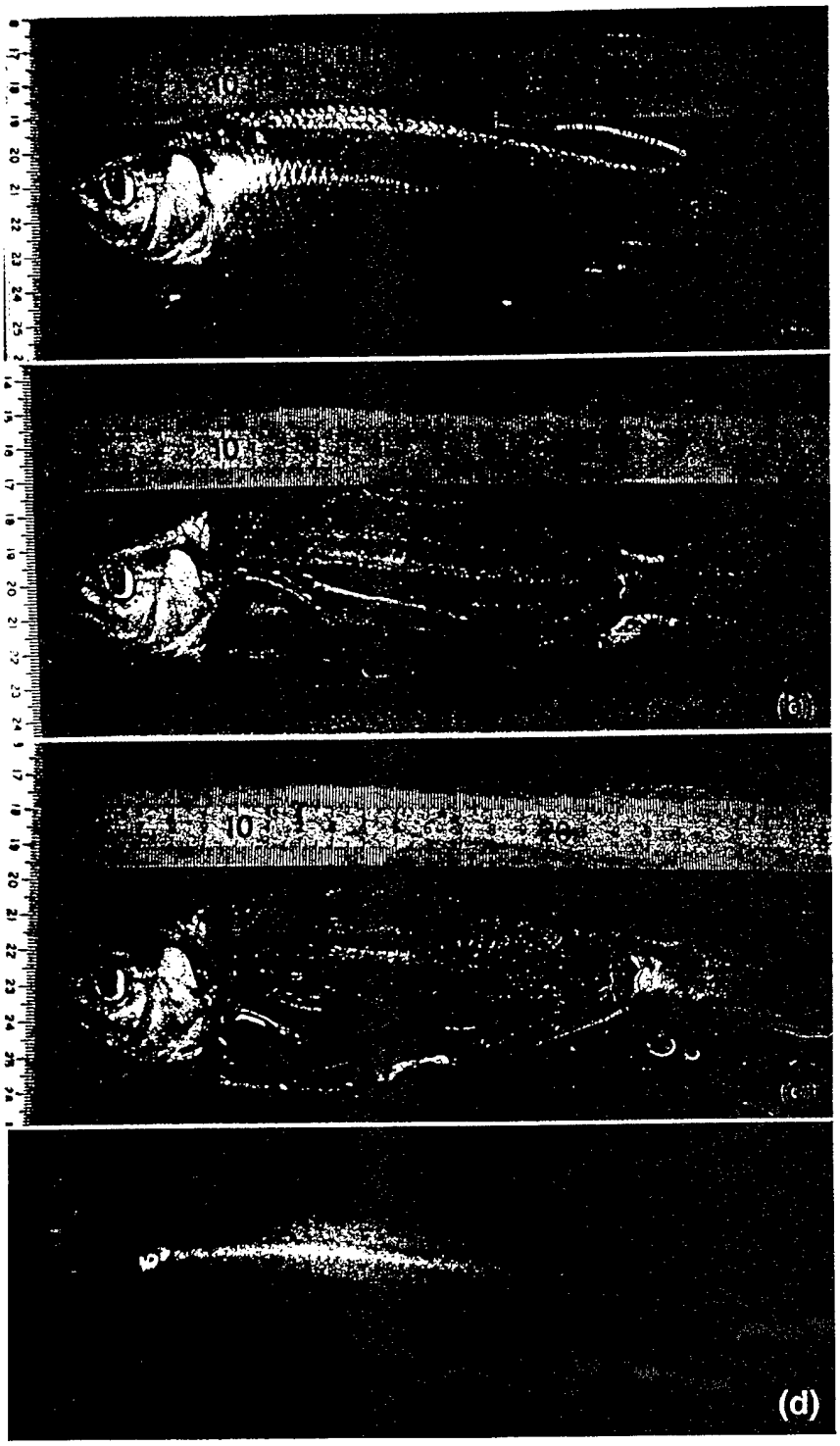


Fig 2

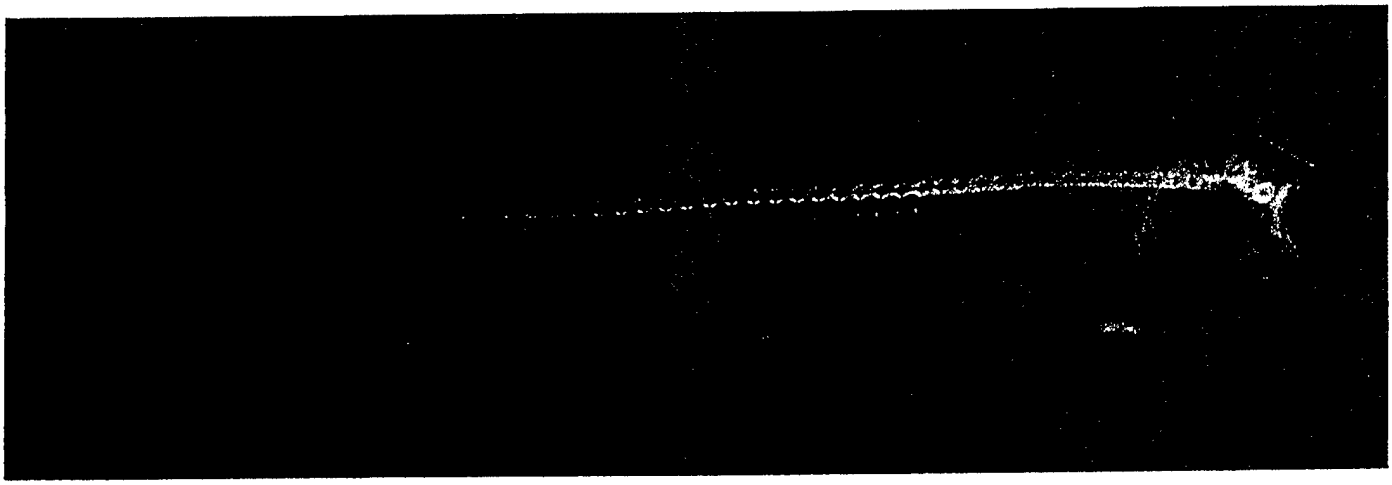

Fig. 3

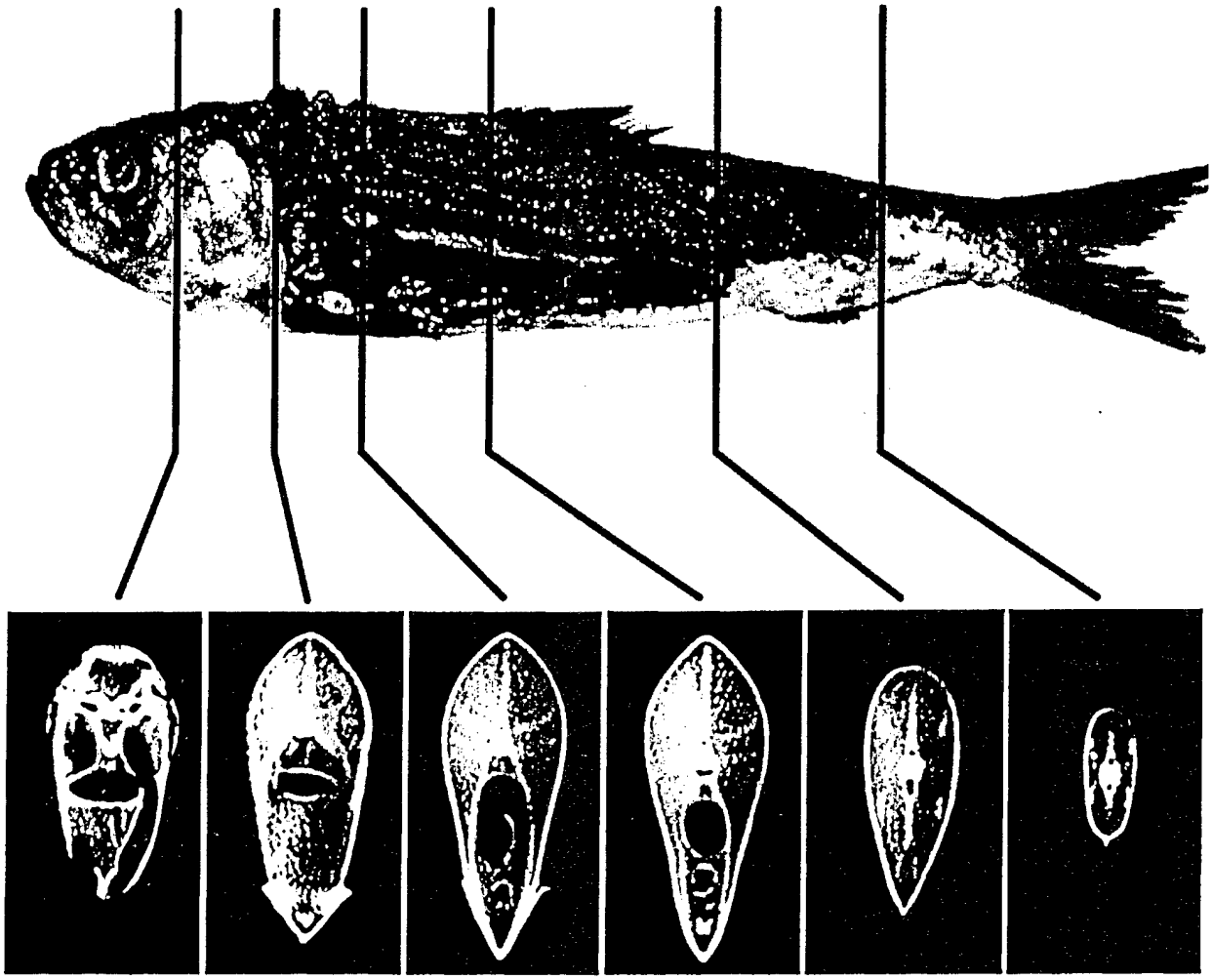

Fig 4

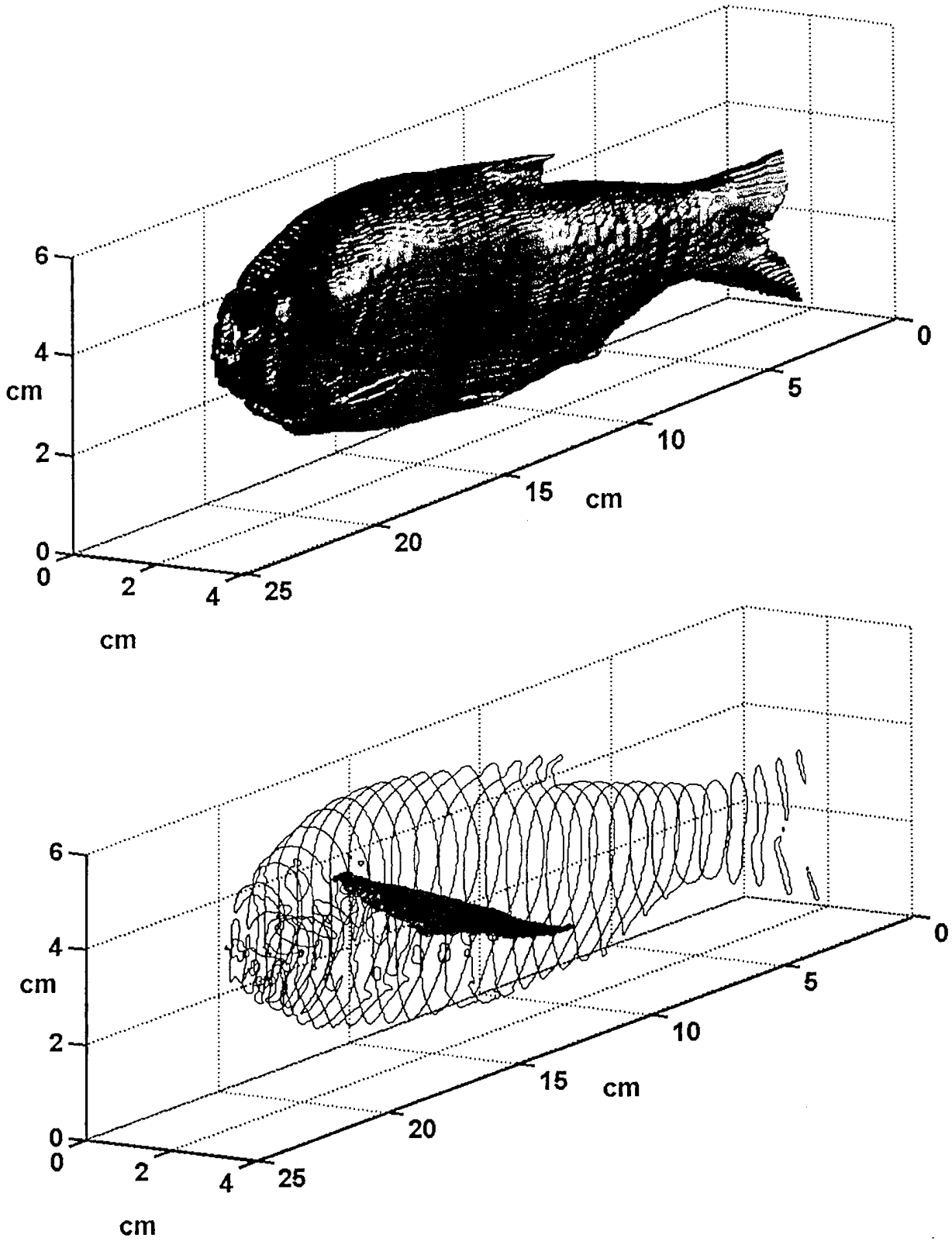


Fig 5

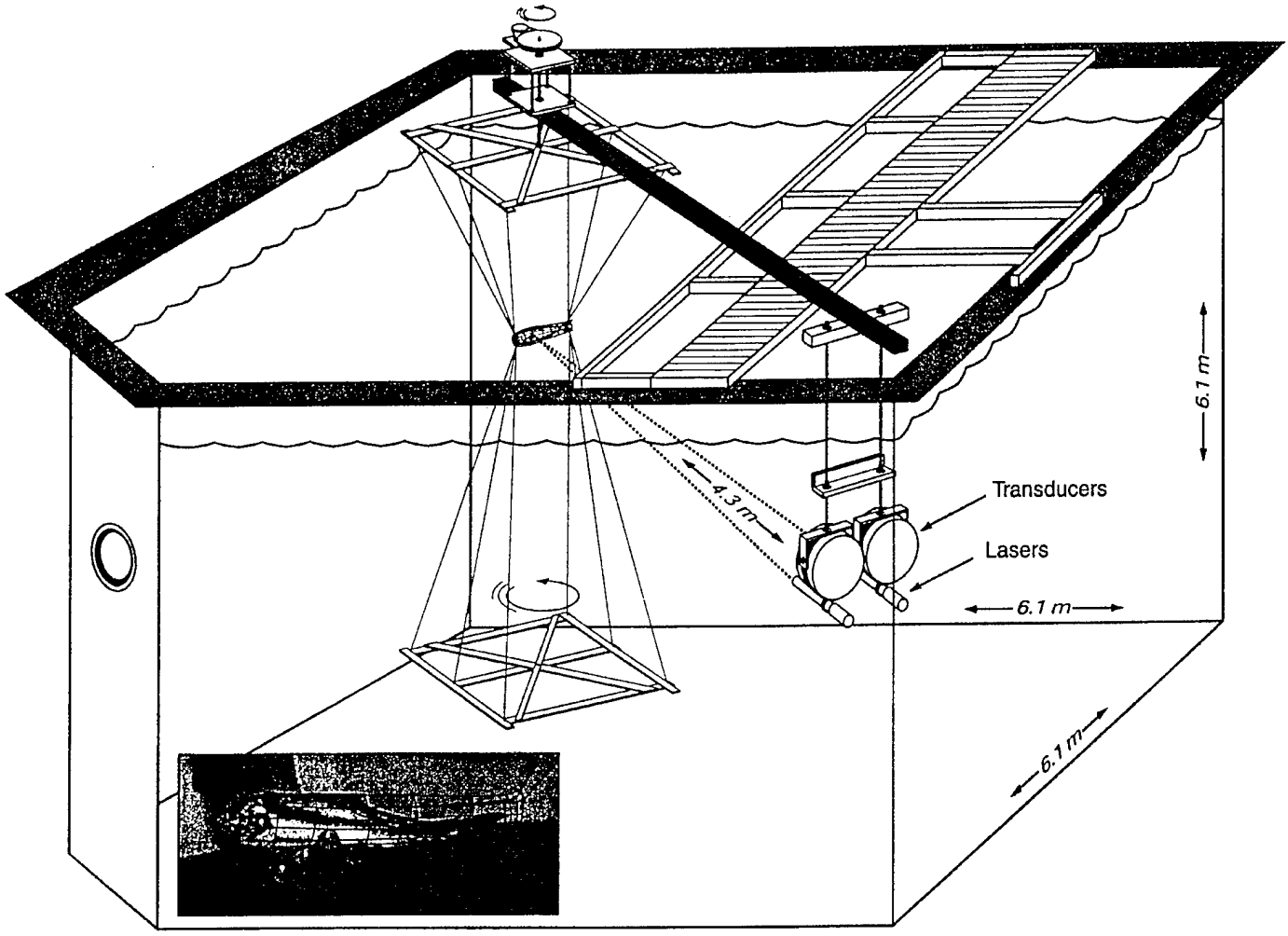


Fig 6

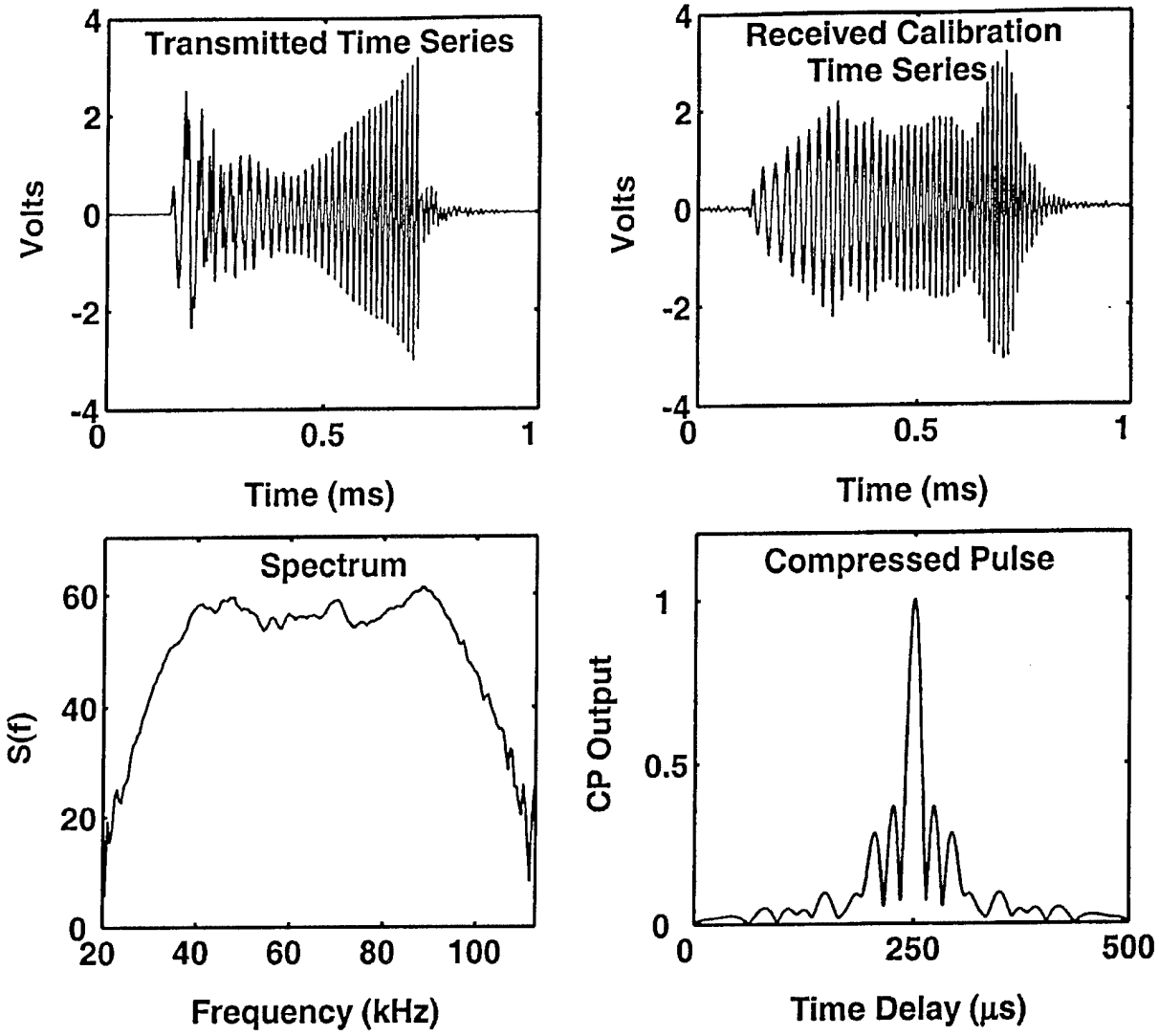
Transmitted Time Series
Volts
Time (ms)
Received Calibration Time Series
Volts
Time (ms)
Spectrum
S(f)
Frequency (kHz)
Compressed Pulse
CP Output
Time Delay (μs)

Fig 7

**Alewife 26**

**Lateral Plane**

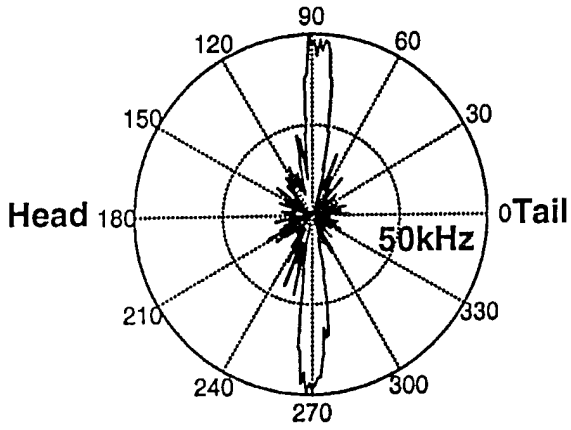


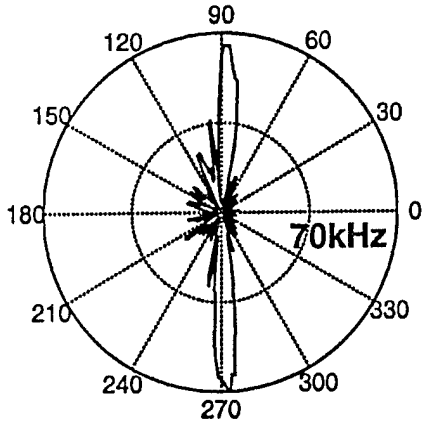


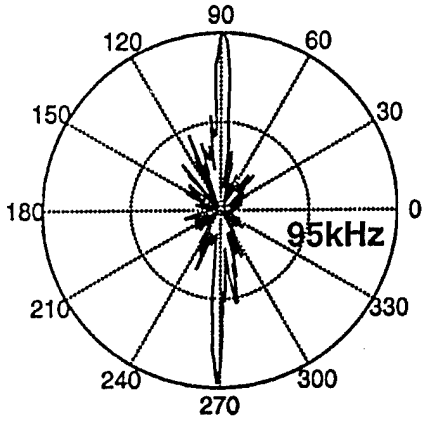


Fig 8

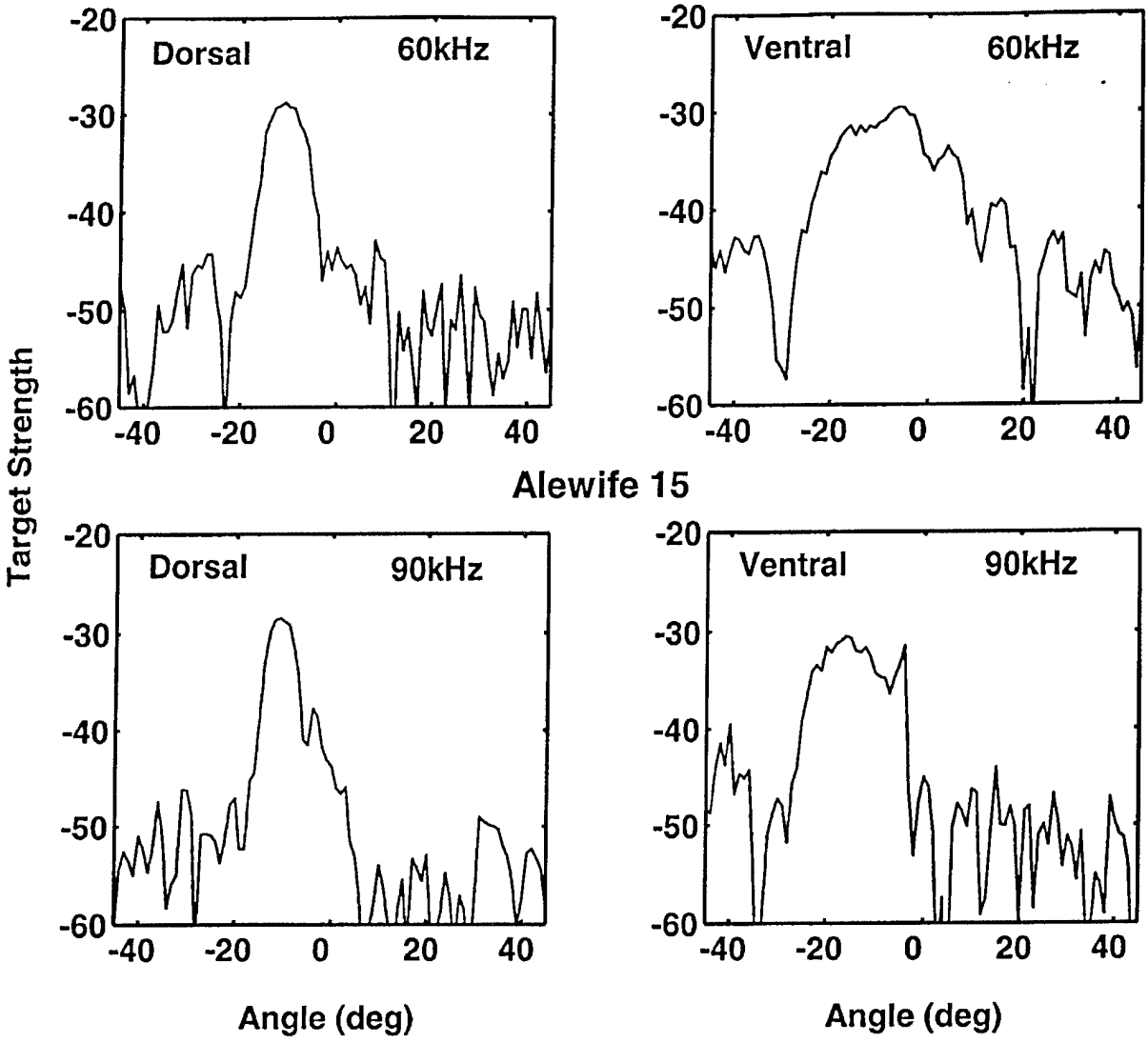
Dorsal
60kHz
Ventral
60kHz
Alewife 15
Dorsal
90kHz
Ventral
90kHz
Target Strength
Angle (deg)
Angle (deg)
-20
-30
-40
-50
-60
-40
-20
0
20
40

Fig 9

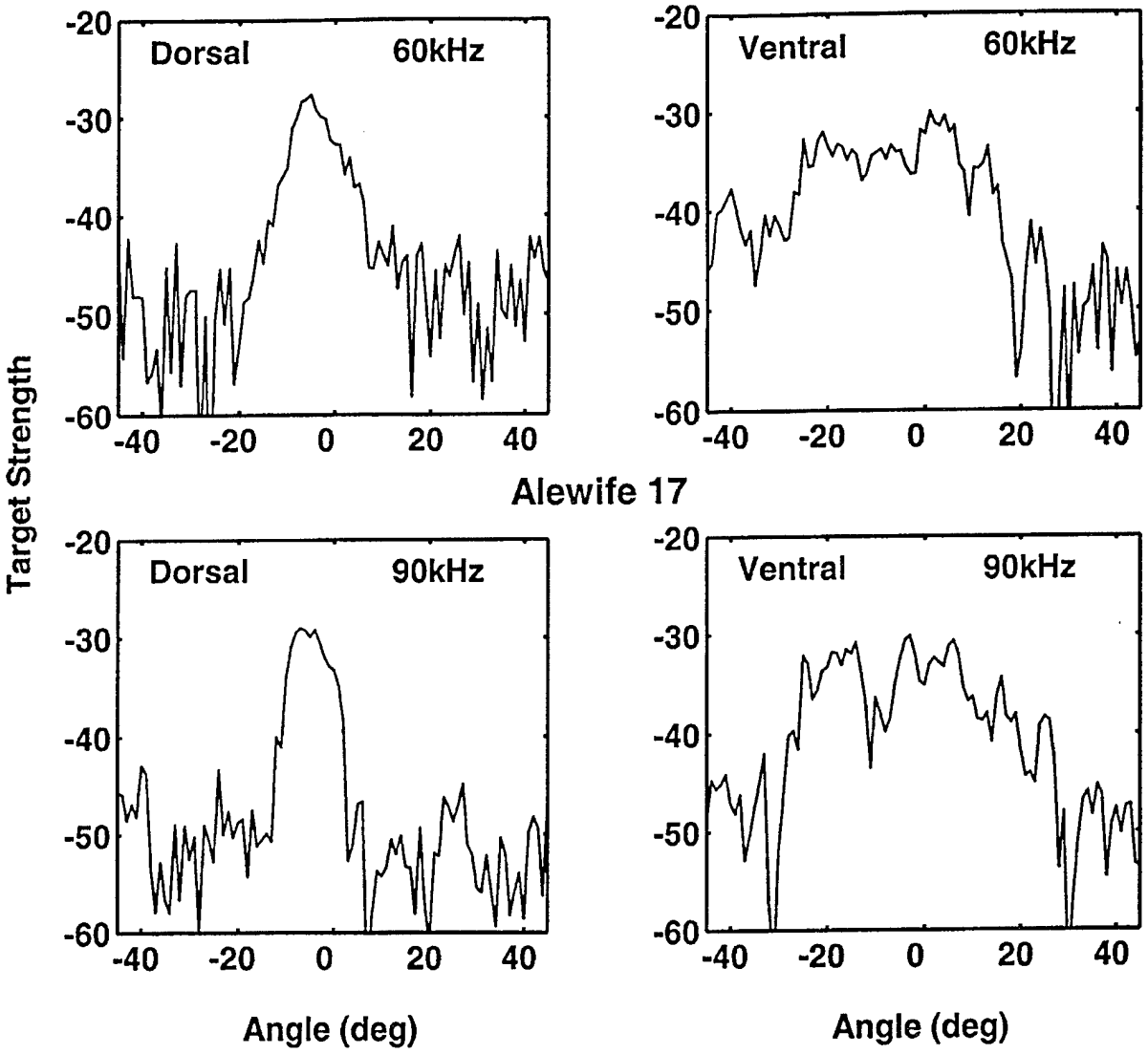
Dorsal 60kHz
Ventral 60kHz
Alewife 17
Dorsal 90kHz
Ventral 90kHz
Target Strength
Angle (deg)
Angle (deg)
-20
-30
-40
-50
-60
-40
-20
0
20
40

Fig 10

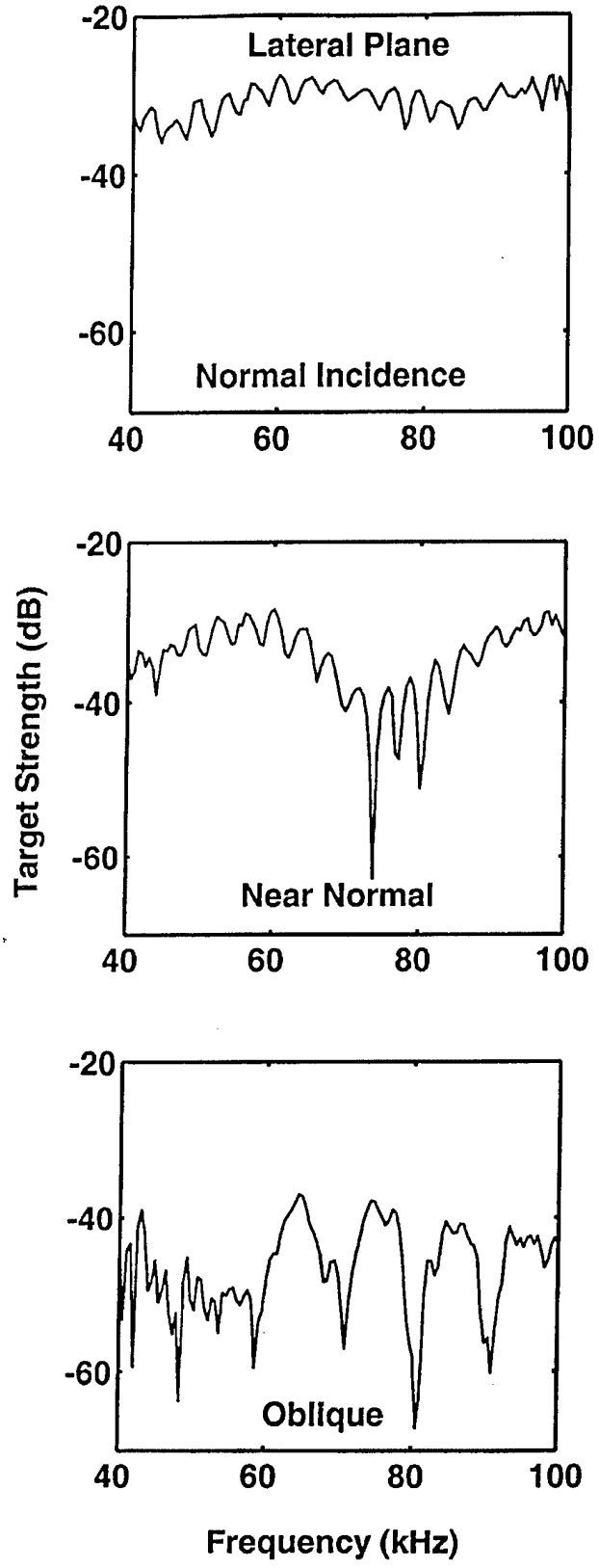
-20
Lateral Plane
-40
-60
Normal Incidence
40
60
80
100
-20
Target Strength (dB)
-40
-60
Near Normal
40
60
80
100
-20
-40
-60
Oblique
40
60
80
100
Frequency (kHz)

Fig 11

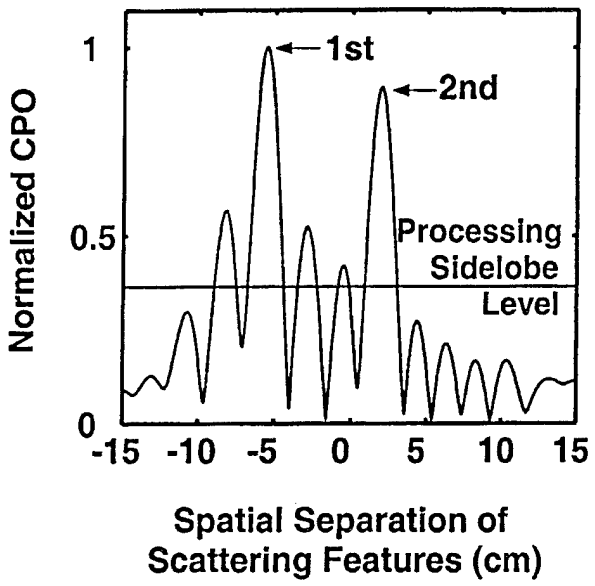
1st
2nd
Processing
Sidelobe
Level
Normalized CPO
1
0.5
0
-15
-10
-5
0
5
10
15
Spatial Separation of
Scattering Features (cm)

Fig 12

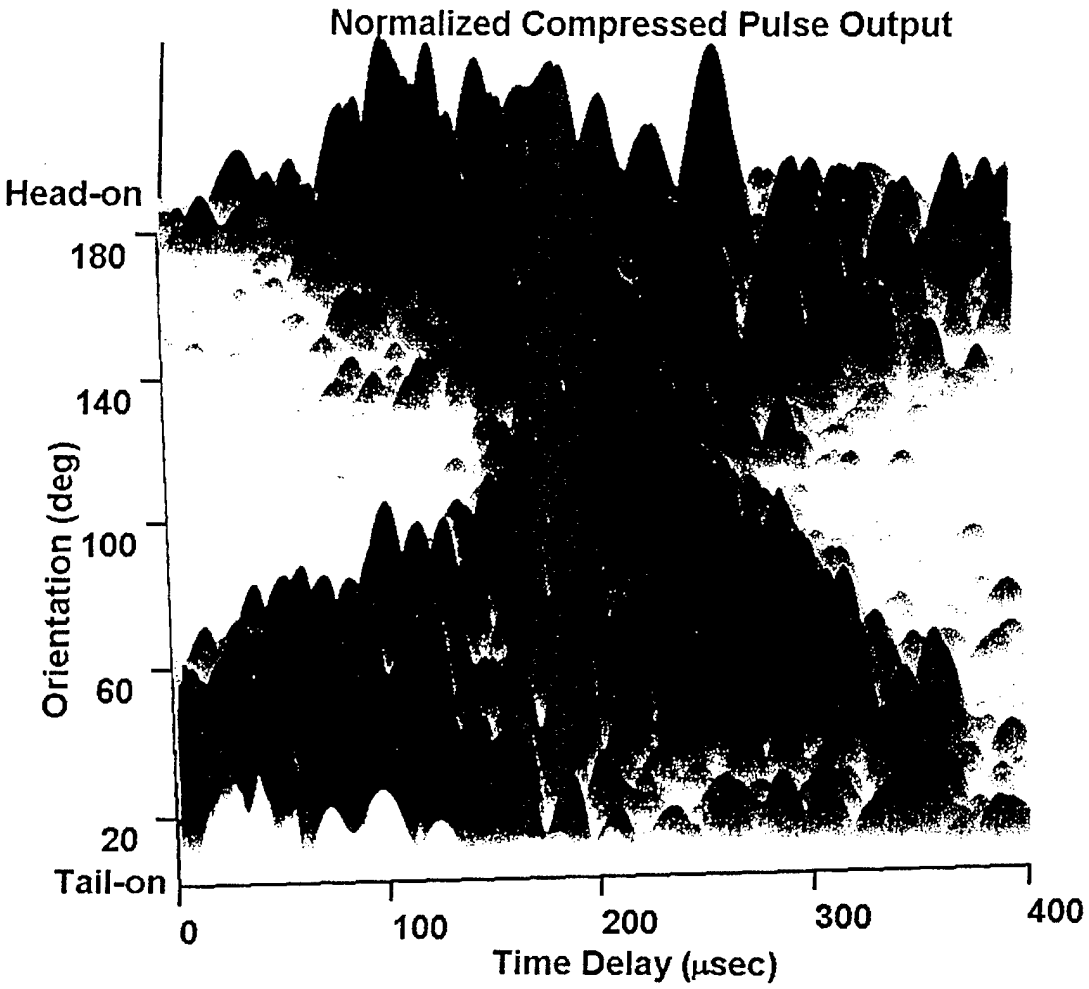
Normalized Compressed Pulse Output
Head-on
180
140
100
60
20
Tail-on
Orientation (deg)
0
100
200
300
400
Time Delay (μsec)

Fig 13

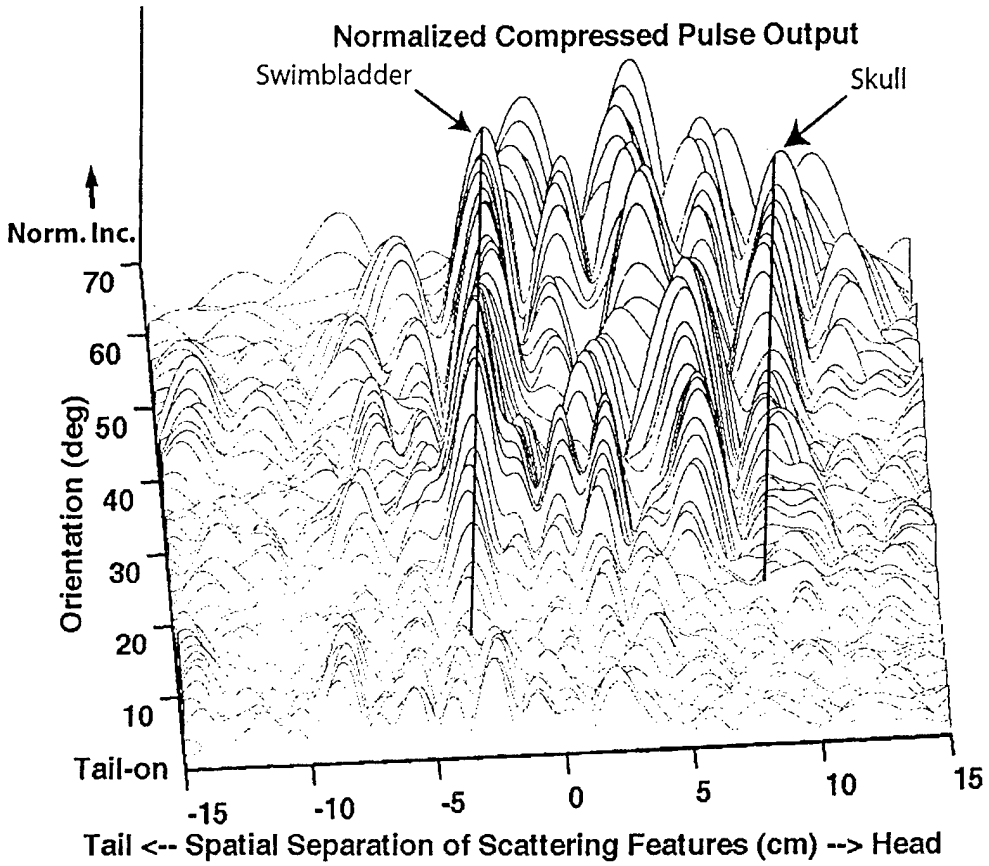
Normalized Compressed Pulse Output
Swimbladder
Skull
Norm. Inc.
Orientation (deg)
70
60
50
40
30
20
10
Tail-on
-15
-10
-5
0
5
10
15
Tail <-- Spatial Separation of Scattering Features (cm) --> Head

Fig 14

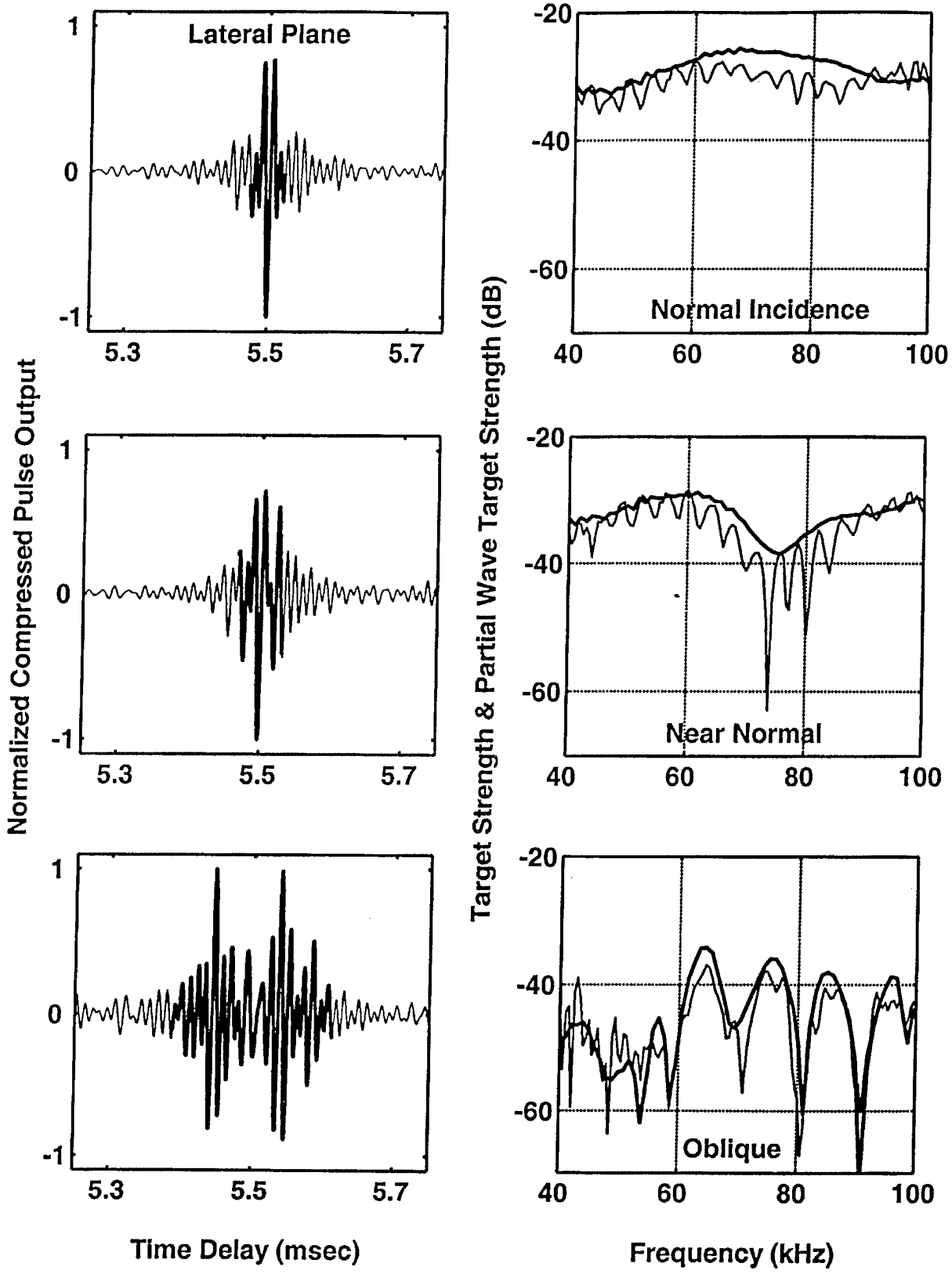
Lateral Plane
Normal Incidence
Near Normal
Oblique
Normalized Compressed Pulse Output
Target Strength & Partial Wave Target Strength (dB)
Time Delay (msec)
Frequency (kHz)
1
0
-1
5.3
5.5
5.7
-20
-40
-60
40
60
80
100

Fig 15

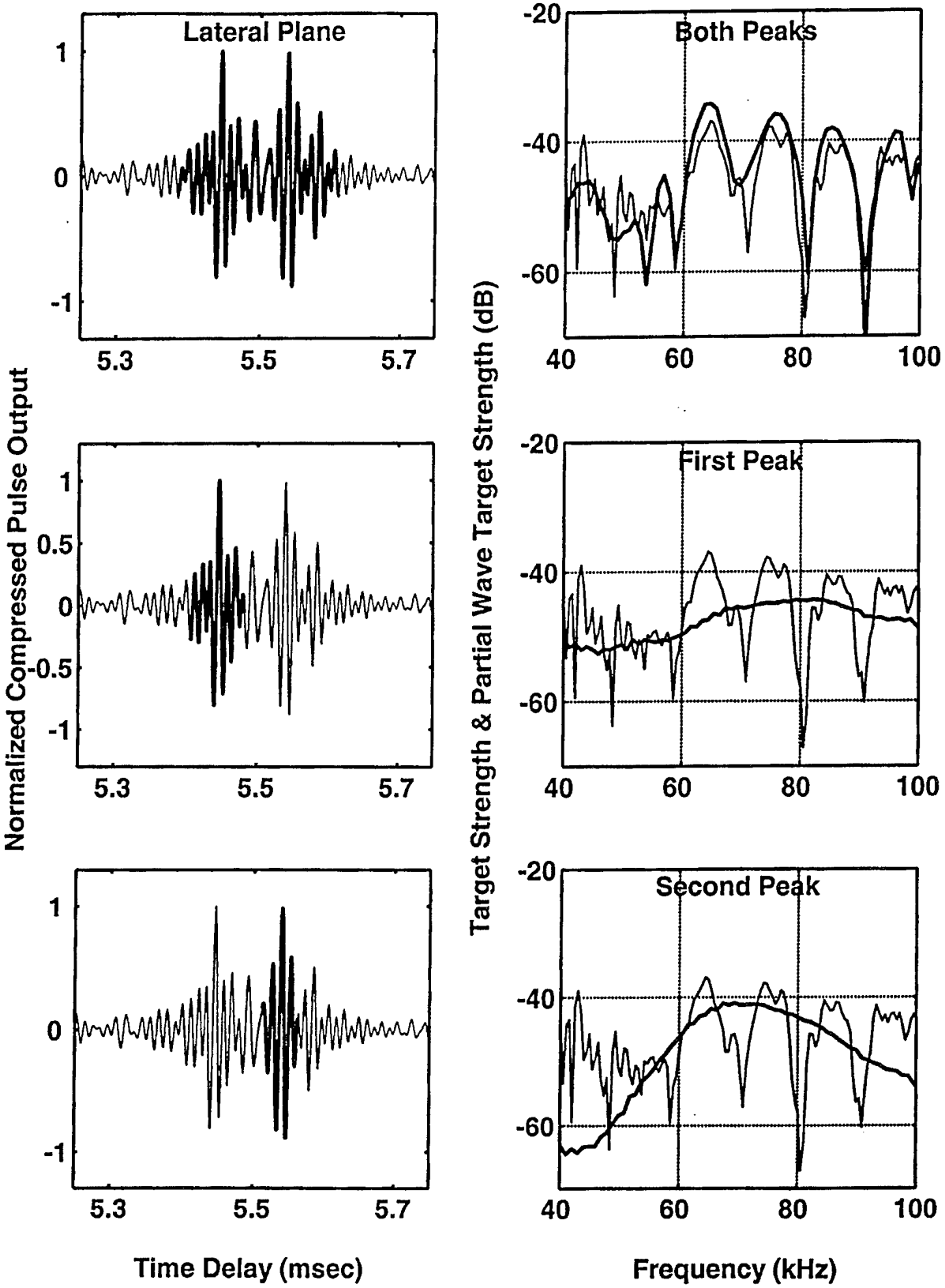
Lateral Plane
Both Peaks
First Peak
Second Peak
Normalized Compressed Pulse Output
Target Strength & Partial Wave Target Strength (dB)
Time Delay (msec)
Frequency (kHz)
1
0
-1
0.5
-0.5
5.3
5.5
5.7
-20
-40
-60
40
60
80
100

Fig 16

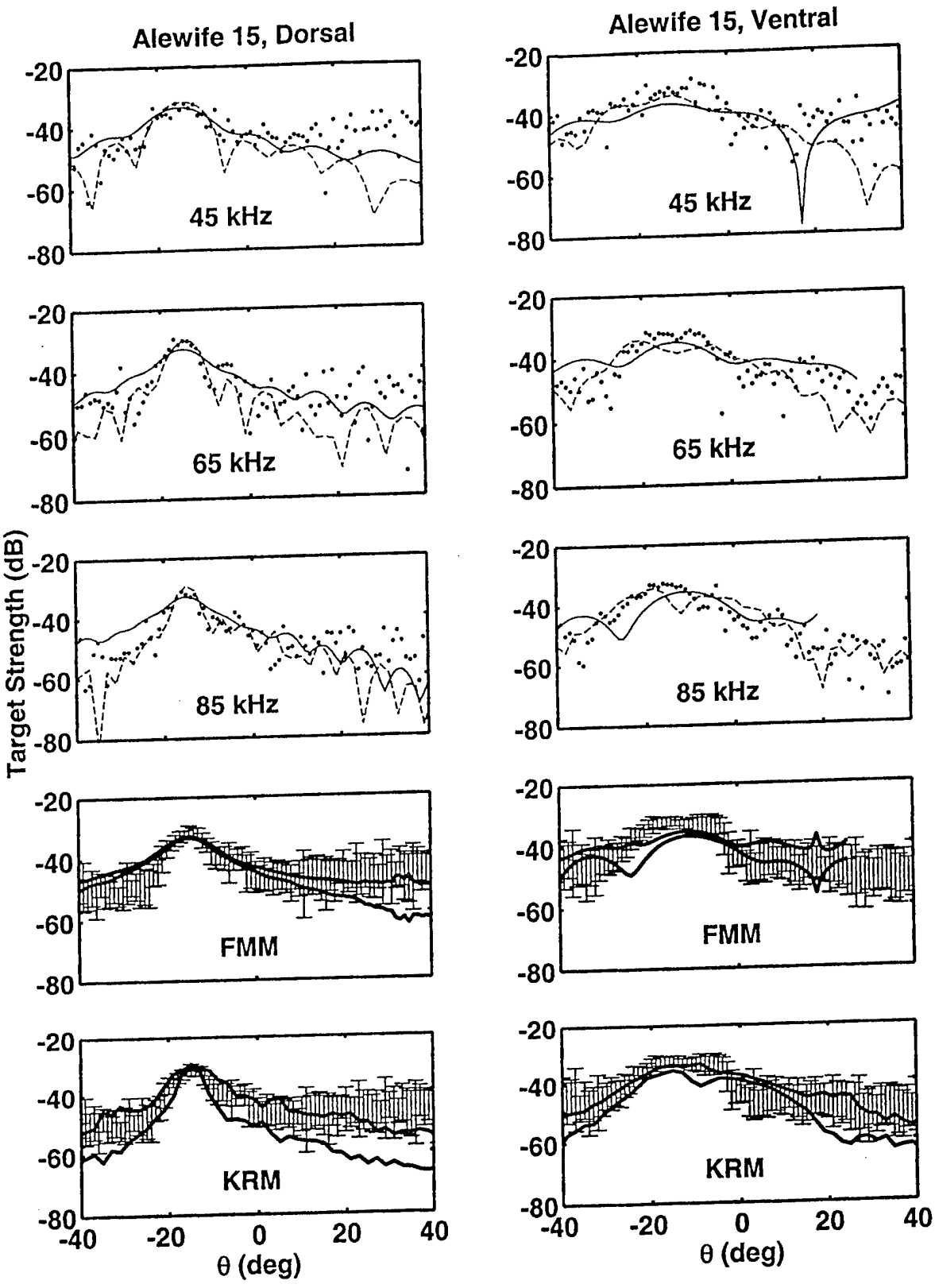
Alewife 15, Dorsal
Alewife 15, Ventral
Target Strength (dB)
-20
-40
-60
-80
45 kHz
65 kHz
85 kHz
FMM
KRM
-40
-20
0
20
40
θ (deg)

Fig 17